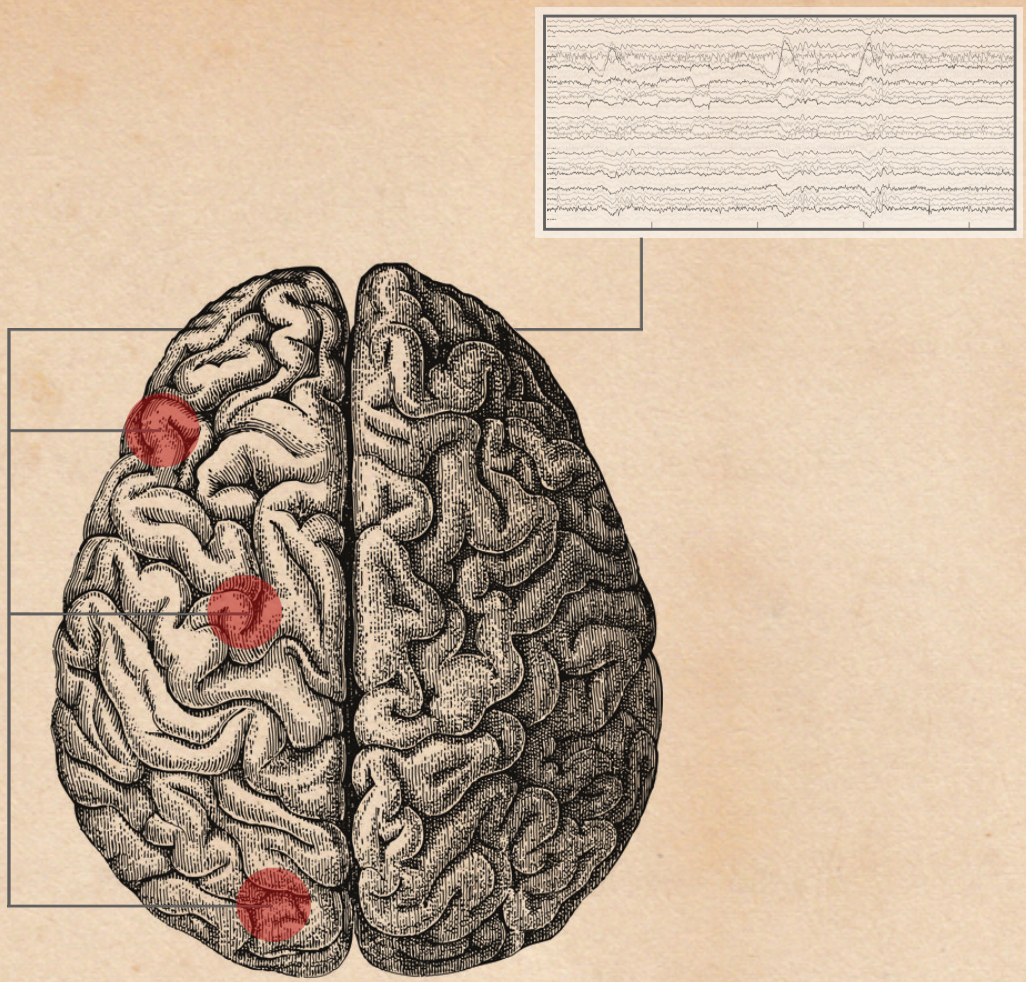

Separating individual finger activity when performing force tasks using EEG source localization methods

Author	Nikolaos Vardalakis
Student Nr.	4744063
Supervisors	Alfred C. Schouten, Dir. ir. Jinne Geelen, PhD Candidate
External Commitee Members	Borbála Hunyadi, dr.

Acknowledgements

I would like to thank my supervisors, Dr.ir. Alfred C. Schouten and Ph.D. Candidate Jinne Geelen, for their gracious support and guidance during the experiment and the writing phases of my thesis project. My colleagues and friends, Chris Christoforidis and Katerina Isaakidou, were very supportive during the difficult stages of my research and I thank them both. I would also like to thank my sister, Katerina Vardalaki, and my close friend Vasileios Skrekas for their support during the writing phase of the thesis. This work is the conclusion of a 2-year long academic journey and thus, I would like to thank all my friends for being part of it. To you I wish all the best with your future career and I am extremely grateful to have you in my life.

This page would be intentionally left blank
if we would not wish to inform about that.

Separating individual finger activity when performing force tasks using EEG source localization methods

Nikolaos Vardalakis*
Delft University of Technology

February 9, 2020

Electroencephalography (EEG) source localization has been applied in the development of brain-computer interfaces to control hand prostheses. When performing fine movements, our brain uses sensory feedback regarding position, velocity, and force to improve performance. Understanding the cortical mechanisms underlying individual finger movements can lead to a higher number of degrees of freedom (DoF) when developing BCI-controlled hand prostheses. Our goal was to test the efficacy of separating the activity of two individual fingers during a pinch-and-hold motor task using EEG source localization.
EEG data from three healthy participants performing the motor task using different fingers were collected and analyzed using two parametric and two non-parametric source localization methods. A statistical analysis was performed on the source space to test whether it is possible to distinguish between the two fingers.
We were able to measure the cortical response to the perturbations on the channel level during the hold phase of the motor task. However, source power in the primary motor (M1) and somatosensory (S1) cortices was low for all conditions. The most active sources were found in the frontal cortex over Brodmann area 8. A cluster-based permutation test performed on the source space results did not reveal differences between the two fingers on the cortical area. Statistically significant ($p < 0.05$) source differences are reported in one case, however, the locations of the sources indicate this effect is irrelevant to the motor task. Our findings indicate that there are no measurable source-level differences regarding the motor activity of individual fingers during the hold phase of the motor task, independently of the source localization method used.

Keywords: **Source localization; Motor control; BCI; EEG; FieldTrip;**

I. Introduction

Electroencephalography (EEG) is used to measure the electrical activity of the brain using electrodes placed on the scalp. The electrodes measure the voltage potential at various locations on the scalp. These measurements are in the order of microvolts (μV). EEG is non-invasive, portable, and demonstrates high temporal resolution in the order of milliseconds [1].

EEG can be used to measure and identify the activation patterns of neural patches. The current produced by a single neuron is not powerful enough to be detected, however, the currents produced from multiple neurons firing are superimposed and whenever neurons fire in a synchronous manner, their activity is measured using EEG [2]. Neural activity can be approximated by current dipoles [3]. The current of the dipoles produces potential differences as it propagates across tissues. These potential changes are measured from the scalp using EEG and can be spatially and temporally localized inside the brain or on its cortical surface [3–5]. The localization process is also termed as the EEG inverse problem in the literature.

The EEG inverse problem is ill-posed; the number of dipole sources is larger than the number of EEG electrodes, thus the solution is non-unique, and the solution is susceptible to noise and small changes in the data, thus is unstable [6]. To obtain a unique solution, prior information regarding the source characteristics or physiological assumptions need to be made to constraint the solution space. Using the recorded EEG and a forward model of the head, one can work backward and solve the inverse problem by estimating the location, orientation, and strength of the current dipole sources which explain the measurements. Localizing the dipole sources gives an estimate of the changes in neural activity of the brain across time. The accuracy of the results is dependent on several factors, such as the noise level and the modeling errors of the head [7–9], and the errors in the source model [6]. In the literature, this process is called source localization.

Two main approaches to solving the inverse problem are presented in the literature: parametric and non-parametric methods. Parametric methods typically assume a small number of active sources, which can

*E-mail: N.Vardalakis@student.tudelft.nl

be represented as current dipoles of unknown strength, orientation, and location inside the brain. In contrast, non-parametric methods assume a large number of dipoles distributed across the brain volume. Their locations are fixed and therefore their strengths and possibly their orientations are to be estimated.

EEG-based BCIs are communication systems that measure brain activity using EEG and use the signals from the electrodes to interface with a computer or another external device [10]. Patients who suffer from impaired movement can use BCIs to control external devices using their neural activity. This is especially important to amputees and those who suffer from severe paralysis [11]. Using a BCI to control an external prosthesis, patients with impaired motor functions have successfully regained some degree of movement through motor prostheses [12–14]. As an example, a recent study reported that a tetraplegic patient was able to walk again through the use of a BCI-controlled exoskeleton [15].

In the literature, source localization techniques have been used to distinguish between left and right-hand movements [16, 17]. EEG source localization techniques have also been used to separate between both real and imaginary movements of the index finger of the left and right hand [12]. These techniques provide some degree of control to the patients and restore parts of their functionality, however only a limited range of movements and attempted movements is effectively decoded, severely limiting the degrees of freedom (DoF) of the end prosthesis. It is possible to improve the quality of motor prostheses by increasing the controlled degrees of freedom using source localization methods of high spatial accuracy, allowing for the detection of active current sources of proximity. This approach holds promise since motor functions are organized somatotopically in the motor cortex [18].

Source localization methods have been used in the literature to develop brain-computer interfaces (BCI). Decoding and replicating highly dexterous motor control in a hand prosthesis, such as individual finger movements, is a challenging task that would improve the quality and performance of the prosthesis. The area of the brain related to the movement of the hand and the fingers has a large representation in the primary motor cortex (M1). Furthermore, individual fingers are controlled by different areas in the M1, which are spatially separated and clearly distinguishable using fMRI [19]. EEG source localization methods with high spatial accuracy are useful in spatially separating the sources responsible for the individual movement of the fingers from the cortical area of the hand in the M1. Being able to distinguish between the movement of the index and the ring fingers increases the available DoF in a hand prosthesis.

In the literature, a few researchers have used source localization to investigate brain activity during finger movements. Some attention has been focused on localizing the motor or event-related potentials (ERP) arising from cued commands [20]. This approach is used both for time and frequency analyses. The analysis of motor EEG data in the frequency domain has proven there is a robust effect in both the beta and the gamma bands related to motor planning and execution [21]. Power in the beta band has been shown to decrease 500 ms before movement onset, an effect that lasts until the movement is executed. A subsequent power increase is also reported 300 to 1000 ms after movement onset. In the literature, these events are termed as event-related desynchronizations (ERD) and synchronizations (ERS) respectively [22].

While the peri-motor time window has been thoroughly studied, the connection between the activity of the brain and the application of a constant force over time, such as individual finger flexion during pinch and hold tasks, has yet to be investigated. It is interesting to investigate the cortical behavior during constant force production, as any findings can lead to more advanced hand prostheses, which can simulate the biological behavior of the human hand and individual fingers during pinch and hold tasks.

In this study, we investigated the feasibility of applying EEG source localization methods to accurately distinguish movements of the index and the ring fingers of the right hand in healthy participants. A motor experiment was designed and EEG data were recorded from healthy participants while they performed a pinch and hold task using two individual fingers of the right hand. Both cases were tested with and without perturbations. The perturbations were included to increase the cortical contribution of the M1 and investigate the effect of the perturbation on the sensorimotor response. The active sources in the brain were localized using four different source localization methods, two parametric and two non-parametric; we selected the methods based on their accuracy, as reviewed in the literature survey. A statistical test was performed on the source-space results of each method to test whether it is possible to distinguish between the use of the index finger and the ring finger for both the perturbed and the unperturbed conditions.

II. Materials and Methods

Subjects

Seven healthy right-handed subjects (aged between 22 and 29 years; all males) participated in the experiment. Participants were M.Sc. students recruited from the Biomedical Engineering faculty of the Delft University of Technology. All participants provided written consent after they were informed about the experimental procedure and were allowed to ask questions. The study protocol was approved by the ethics committee of the university.

Experimental protocol

During the experimental sessions, participants were seated comfortably in a padded chair 150cm away from a computer screen. Their right forearm was placed on top of an arm support and movement of the wrist joint was prevented using a wrist brace. This position prevented the excessive movement of the forearm and the wrist during trials, while allowing the free movement of the index and ring fingers. The movement of the thumb was constrained by the stationary indentation of the haptic interface, whereas the controlling finger was placed in the opposite, movable indentation. The device offers adjustable stiffness, mass, and damping and was designed at the TU Delft by Cristiansson [23]. The position of the controlling finger and the applied forces are measured by a Linear Position Transducer (Schaevitz 2000 LCIT) and a Tension/Compression Load Cell (FUTEK L2357+JM-2A) respectively. The complete setup is shown in **Figure 1**.

Participants were instructed to perform a series of force tasks using their index and ring fingers in succession. They were first trained to apply a force by flexing the controlling finger to match the target force level shown on the screen. During the trials, participants were asked to apply a pinching force by flexing the controlling finger (either index or ring), thus moving the sliding lever of the robot. Visual feedback was projected on the screen. The target force was set to 12 N, a value well within the physiological limits for young males [24]. A horizontal line on the screen indicated the target force that the participants had to reach. The force applied by the participants was measured by the force sensor and plotted in real-time against the reference.

In total, participants completed 5 conditions; a resting state measurement and 4 different force tasks (2 using the index finger and 2 using the ring finger). Participants performed each condition once, where each force condition consisted of 50 trials and the resting condition was measured continuously for 1 minute. The total number of performed force trials was 200. Participants completed the resting measurement first, followed by the force conditions presented in random order. No two participants performed the same order of conditions during their experiments. All conditions were preceded by a short 10-trial training session to familiarize participants with the condition. Participants were given a short 1-minute break after 25 consecutive trials per condition. Upon completing all 50 trials for each condition, participants were allowed to have a 5-minute break to prevent fatigue.

Force tasks were performed with and without position perturbations. During a force task, participants are required to maintain a constant force output irrespective of the position of the joint. Position perturbations force participants to control in such a way that minimizes the effect of the position change in the applied force [25]. Force feedback is useful and thus, the activity of the somatosensory cortex is expected to increase. The designed position perturbations were random-phase multisine signals (i.e. the sum of multiple sinusoids of random phase and a certain frequency). Multisine perturbations are preferable over random signals, since the excited frequencies are controlled precisely, which offers numerous advantages in system identification [25].

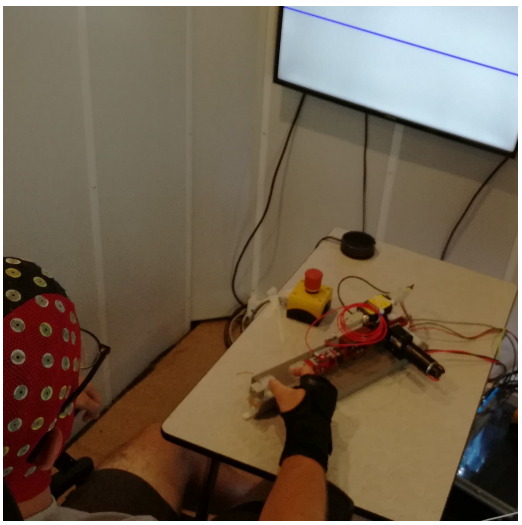

(a) *Complete setup*

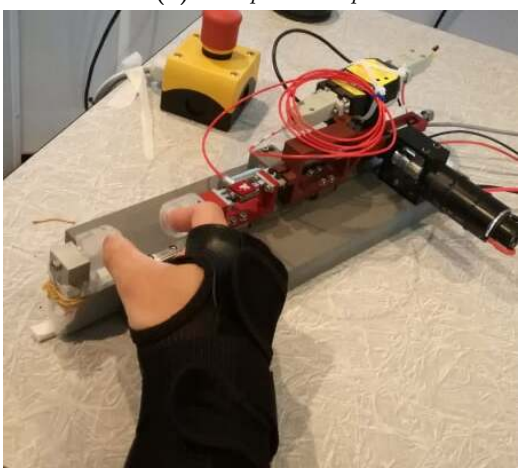

(b) *Hand position in detail*

Figure 1: *During the experiment, participants were fitted with the 128-channel EEG cap and seated comfortably in a chair. Their right arm was resting on the arm of the chair. The reference signal and the applied force, as measured by the haptic interface, were plotted in real-time on the computer screen in front of them. The placement of the fingers and the wrist is presented in more detail in the bottom image. The thumb was placed on the immovable indentation and the controlling finger (the index in this case) was placed in a similar indentation on the movable arm of the robot. An emergency button which stops the experiment was placed within reach of the left arm of the subject.*

The position perturbations were multisine signals with a peak-to-peak amplitude of 2 cm around the resting position x_0, with a period T of 1 second and a fundamental frequency f_0 of 1 Hz. Both odd and even

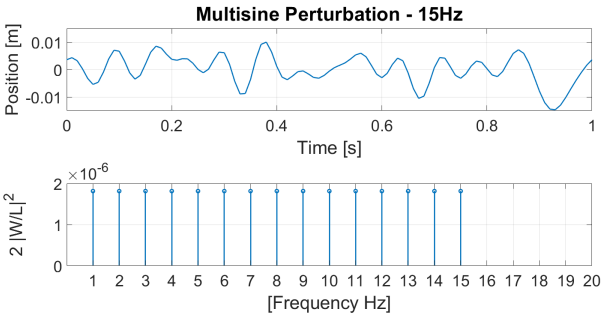

Figure 2: *The perturbation signal used during the experimental procedure. The signal is made up of 15 random-phase sinusoidal components, each having a different frequency across the whole integer range of 1 to* 15 *Hz. This signal is periodic with* $T = 1$ *seconds. For the perturbed trials, the position perturbation consists of 6 periods of the base multisine signal, which adds up to 6 seconds in total.*

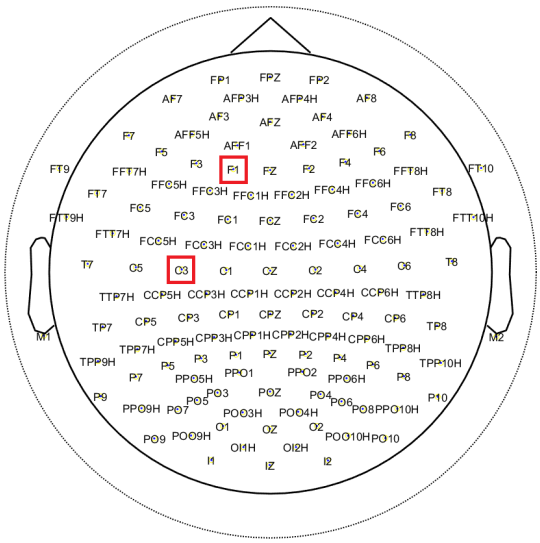

Figure 3: *The layout topology of the EEG cap used during the experiments. The channels are projected from 3D to 2D. Due to the projection, some of the electrodes appear to be placed outside the head circle. The outer circular boundary corresponds to the covered area of the electrodes. The closer an electrode is to the edge of the outer circle, the lower its placement on the 3D head. We used the WaveGuard EEG cap by AntNeuro which features 128 channels. Two channels are marked: the F1 and the C3. These two channels were chosen for further analysis and are highlighted for future reference.*

harmonics of the fundamental frequency were excited in the range $[1, 15]$ Hz. The signal was designed to have the same power in each frequency bin. A single realization of the multisine signal was generated; the complete perturbation signal had a length of 6 seconds, leading to 6 periods per trial and a total of 300 periods per condition. The signal is presented in **Figure 2** both in time and in frequency domain.

Participants were fitted with an EEG cap with 128 electrodes (Waveguard 128). The cap is following the 10-5 system [26]. The layout of the cap is shown in **Figure 3**. Cortical activity was recorded at 2 kHz from 126 electrodes using an EEG amplifier (Refa by TMSi, Oldenzaal, The Netherlands). The position of the controlling finger, the applied force, and the initiation trigger were also recorded through the amplifier via a galvanic isolator transformer (TMSi, Oldenzaal, The Netherlands). The signals were recorded using the ASALab software.

EEG Preprocessing

EEG data were preprocessed using the FieldTrip toolbox, developed by the Donders Center for Cognitive Neuroimaging [27]. The preprocessing pipeline is an adaptation of Makoto's preprocessing pipeline for EEGlab [28].

Three complete datasets were used in the study. The rest were discarded post-experimentation due to hardware failures and data corruption. In one case, more than 50% of the total trials had to be discarded as the participant moved before the experiment started. In two other cases, a faulty lead in the EEG cap caused only noise and artifacts to be recorded for some conditions. In another case, the recorded data for one condition were incomplete and could not be recovered. In the end, we decided to omit the incomplete datasets to avoid inconsistencies in the analysis.

EEG was recorded continuously during each task. The continuous-time EEG data were band-pass filtered using a finite impulse response (FIR) Hamming-windowed sinc filter. We filtered the data using a forward band-pass filter with an order of 3380 and delay compensation to achieve zero-phase. The passband of the filter was selected as $[1, 100]$ Hz, which removes the baseline drift caused by frequencies $f < 1$ Hz while retaining the neural activity within both the β– and the γ– bands. The continuous EEG was subsequently downsampled to 256 Hz. Next, the continuous EEG was cut into individual trials using the time information of the recorded trigger signals at the start and the end of each trial (epoching).

Individual trials were removed post-epoching, in cases when the participants moved too soon or too late, using the finger position signal recorded from the robotic manipulator. The conditions were grouped based on whether a perturbation was applied or not. The data of each finger were processed together per subject to simplify the following steps of trial and channel rejection and improve the performance and accuracy of the Independent Component Analysis (ICA) [29]. Transient responses were cut out during the analysis. The first and last 1-second intervals from each trial were discarded; for the multisine conditions, this is equivalent to discarding the response to the first and the last periods of the perturbation signal, resulting in a total of 200 1-second periods per

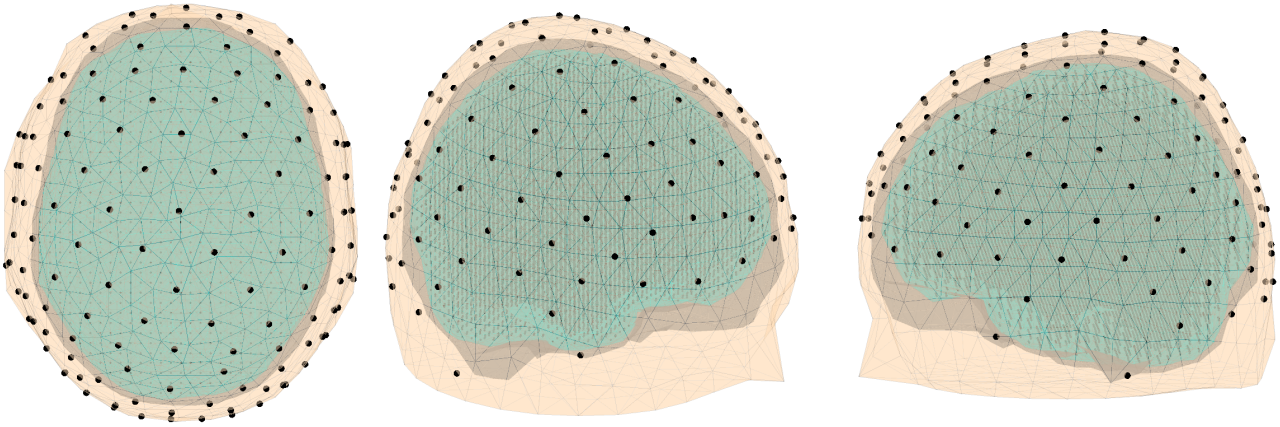

Figure 4: *The three-layer boundary element method (BEM) realistic head model used in the current study. The three layers and their conductivity values are listed from the innermost to outermost: $\sigma_{brain} = 0.33$ S/m, $\sigma_{skull} = 0.0041$ S/m, $\sigma_{scalp} = 0.33$ S/m. The black dots on the top of the scalp denote the position of the channels of the Waveguard 128 EEG cap. Inside the brain (highlighted green layer) the source model is plotted as a grid of points, denoting the positions of the dipole sources in 3D space. The grid resolution is 5mm.*

condition per participant.

The data were visually inspected for EMG artifacts. Noisy trials and corrupted channels were discarded from the dataset. Channels contaminated by noise and glitches were identified both visually and using the approach of Farahani et al. [30] and discarded. Next, the data were re-referenced to the common average of the remaining channels. ICA was performed on the dataset to separate and identify noisy components using the RUNICA implementation provided in FieldTrip; RUNICA is based on the implementation of the algorithm in EEGlab which is a modified implementation of the Infomax ICA decomposition algorithm [28]. The Infomax algorithm is better suited for finding cortical EEG sources than fastICA and thus was chosen to remove blink artifacts from the datasets [31]. The independent components were analyzed in both the time and frequency domains. Components related to the EOG activity were rejected and the remaining components are projected back to the EEG measurement space for each channel. Robust de-meaning was performed on the artifact-free data [32]. To study the steady-state cortical response, the time window of interest per trial was selected as the time window $t_w = [1, 5]$ seconds. The cleaned data structures consist of EEG voltages recorded for 4 conditions from $E \leq 126$ electrodes during $M \leq 50$ trials per condition.

Forward Model

For the current study, a template three-layer boundary element method (BEM) realistic head model was used [33] and the results of the source localization were interpolated on a template MRI [34]. The conductivity values selected for the homogeneous tissues in the model were 0.33 S/m for the scalp (σ_{scalp}) and brain (σ_{brain}) tissues and 0.0041 S/m for the skull (σ_{skull}) tissue. The effects of the choice of tissue conductivity values have been researched and well documented in the literature [9, 35, 36]. The conductivity ratio between the scalp and skull has been shown to affect the localization error more than the individual values of σ_{scalp} and σ_{skull}. In our head model, the chosen values produce a conductivity ratio $\sigma_{scalp}/\sigma_{skull}$ of 80. The sources were scattered across the whole brain volume on a grid with a resolution of 5 mm. The positions of the Waveguard electrodes were aligned on the surface of the skin in 3D using a template layout provided by the FieldTrip toolbox. We applied the 3D iterative closest point (ICP) [37, 38] algorithm on a subset of electrodes along the nasion-inion line and along the C* electrodes to register the two point-clouds in 3D space. After correcting the rotation, translation, and scaling of the electrodes, they were projected on the surface of the skin. The complete head model is presented in **Figure 4**.

Analysis Pipeline

1. Channel-Level

Prior to source localization, the data were analyzed on the channel level in both time and frequency domains. For the conditions with the periodic perturbation, the recorded EEG signals were analyzed across $P = 4$ periods and M repetitions, per the relevant literature [39]. Due to the periodic nature of the perturbation, we can assume the response is also periodic with $T = 1$ second. Any other activity is considered noise. For the conditions without perturbations, the signals were only analyzed across repetitions.

1.1 SNR calculation An estimate of the cortical activity as a response to the perturbation was calculated by computing the signal-to-noise ratio (SNR) for each channel. The SNR was computed for the two conditions for which the perturbation was applied.

This process is described in a relevant study where the wrist joint is perturbed in a similar way [39]. The formulas which will be presented below are adapted from the relevant literature.

In line with the applied periodic perturbation, the steady-state response was cut into $P = 4$ segments of $T = 1$ second duration. The signals were transformed into the frequency domain using the Fourier transform. This resulted in $X^{[e,m,p]}(f)$, where e denotes the electrode, m denotes the trial number, and p denotes the period; $X^{[m,p]}(f)$ is a matrix which contains the Fourier transform of the sampled voltages of all E electrodes for trial number m and period p.

To estimate the power of the signal of each channel, we average the signal of each electrode over periods within each trial in the frequency domain. This reduces the effect of the noise due to the non-periodic parts of the response. The power of the signal is calculated and averaged across trials and summed over all frequencies.

$$\hat{E}_{X,total}(e) = \sum_{f=1}^{F} \frac{1}{M} \sum_{m=1}^{M} \left| \frac{1}{P} \sum_{p=1}^{P} X^{[e,m,p]}(f) \right|^2 \quad (1)$$

To estimate the level of noise, a similar approach was used. Firstly, the variance of the signals in the frequency domain over $P = 4$ periods in each trial is calculated. Next, the variance is averaged across all M trials. Finally, the result is summed across all frequencies.

$$\hat{\sigma}_X^2(e) = \sum_{f=1}^{F} \frac{1}{M} \sum_{m=1}^{M} \frac{1}{P-1} \sum_{p=1}^{P} \left| X^{[e,m,p]}(f) - \frac{1}{P} \sum_{p=1}^{P} X^{[e,m,p]}(f) \right|^2 \quad (2)$$

Having calculated the signal power estimate and the noise level estimate across all channels, the two are divided to get the SNR per channel.

$$\mathrm{SNR}(e) = \frac{\hat{E}_{X,total}(e)}{\hat{\sigma}_X^2(e)} \quad (3)$$

1.2 Time-Frequency analysis The power of the recorded signals per frequency was calculated across time by performing a time-frequency analysis for all conditions using the Morlet wavelet method [27]. The analysis was performed across individual trials and the results were averaged by condition for each participant. The width of the Gaussian used when constructing the wavelet to estimate the phase and amplitude of the signal was 7 cycles. The range of the center frequencies of the wavelet includes all integer frequencies in the range of 1 to 100 Hz. The time window was shifted in 25 ms increments across time points ranging from 5 seconds prior to movement onset until 1-second post-trial completion. The results were visually inspected for movement-related power changes in three individual bands; the alpha (8-12 Hz) [40], beta (14-30 Hz) and gamma (30-100 Hz) bands [21].

2. Source-Space

The results from the source localization methods are sensitive to the selection of the parameters, the accuracy of the forward model, and the level of noise present in the data [6]. The number of localized sources and their power depends largely on the lead field matrix and the selection of the source localization method to be used. To mitigate these effects, we applied four different source localization methods on the cleaned EEG data: two parametric and two non-parametric. Their results were compared for similarities at the source level and identify which produces the most accurate results under our conditions. In the literature, the most used parametric methods are beamforming methods in the time and frequency domain: the linearly constrained minimum variance (LCMV) beamformer [41] and the dynamical imaging of coherent sources (DICS) beamformer [42] respectively. Similarly, the most well-known non-parametric method is the low-resolution electromagnetic tomography (LORETA) [43]. LORETA solutions are blurry and are not suited for spatially separating sources which are closely located. Two improvements upon this method correct this issue: the standardized low-resolution electromagnetic tomography (sLORETA) [44] and the exact low-resolution electromagnetic tomograpgy (eLORETA) [45]. In the present study, the two improved methods were used.

2.1 Parametric methods A beamformer is a spatial filter that filters the EEG data from the electrodes to separate and maintain signals originating from an area of interest [46]. An advantage of this technique is that it requires no prior knowledge regarding the number of dipoles [6]. In the current study, the data were analyzed using the linearly constrained minimum variance (LCMV) beamformer [41], which uses time-domain data for source localization, and the dynamical imaging of coherent sources (DICS) [42] method, which calculates the coherency between active sources and the source power is estimated in the frequency domain [47].

Using LCMV, source power was calculated by computing the neural activity index (NAI). The NAI is computed by normalizing the source power using an estimate of the spatially inhomogeneous noise [27]. Estimating the noise is done using FieldTrip and the estimate is based on the smallest eigenvalue of the covariance matrix. Using the NAI to estimate the source power is necessary to correct for the center-of-head bias due to the lead fields. This can be circumvented by normalizing the columns of the lead field matrix during computation.

An alternative to computing the NAI to correct the depth bias is to contrast two distinct conditions. This can be done in a within-trial fashion, by contrasting the time window of interest to the pre-stimulus baseline, or by contrasting a specific time window across two different conditions i.e. with and without the application of a perturbation. Calculating a common

spatial filter using the data from all the conditions is suggested for this process. Using a common filter, source activity differences can be attributed to differences in power among conditions instead of differences between individual spatial filters. For the LCMV a common filter was calculated for all conditions and the NAI was calculated using the projection of the noise. Due to ICA component rejection, the covariance matrix is not full rank and thus the regularization parameter λ was set to 100%, as proposed in the relevant literature [27].

Using DICS, changes in source power were calculated by comparing the steady-state response to the pre-stimulus baseline in the alpha frequency band. The steady-state response time window was chosen as [1 5] seconds while the baseline was chosen as [-5 -1] seconds, where $t = 0$ marks the trial onset. As in the case of the LCMV beamformer, the regularization parameter was chosen as $\lambda = 100\%$ to correct for the low-rank of the cross-spectral density matrix. The analysis was performed in the alpha frequency band (8-12 Hz) to localize the sources responsible for the suppression of the mu rhythm, centered around 10 Hz with a spectral smoothing of ± 2 Hz.

2.2 Non-parametric methods Low-resolution electromagnetic tomography (LORETA) [43] is a popular method used in source localization, operating under the constraint of smoothly distributed sources across the whole brain volume. The core assumption of this method is that neighboring neurons are activated simultaneously and synchronously. The method normalizes the columns of the lead field matrix to correct for the depth bias of other methods. However, it produces blurry source estimates due to the initial assumption. Experiments have shown that this method is not suitable for focal source estimation due to spurious brain activity [48].

Standardized low-resolution electromagnetic tomography (sLORETA) is a method based on the minimum norm solution. The inverse solution is obtained by calculating the minimum-norm estimate of the current density and standardizing it using its variance. This variance in the current density is attributed to the actual variance of the sources and the noise present in the EEG measurements. The sLORETA method is reported to produce a zero localization error [44]. This method gives the lowest localization error as reported in the literature [6, 21, 44].

Exact low resolution brain electromagnetic tomography (eLORETA) [45] is another advanced method, based on the weighted minimum norm inverse solution. It computes the cortical current density distribution in 3D space. In eLORETA, the specific weights that are used in the method allow for the exact localization of focal test sources, providing solutions with exact localization yet low spatial resolution. This is inherent to all LORETA variants and is based on the physiological assumption that neighboring neuronal sources are highly correlated. The eLORETA method is an improvement of sLORETA as it has been shown to have zero localization bias in the presence of structured noise.

All of the above methods are greatly affected by regularization. When computing the inverse solution, the regularization parameter λ needs to be specified. Since our source estimates were calculated from the reconstructed EEG data post-ICA component rejection, the data matrix is rank-deficient and therefore regularization is necessary. For the LCMV case, a low-rank covariance matrix greatly deteriorates the quality of the solution to that of a minimum-norm estimate [49]. It is possible to circumvent this issue by using sLORETA/eLORETA instead of the LCMV beamformer. However, regularization is beneficial for LORETA variants as it reduces both blurriness and false positives [6]. Due to the above and since artifacts were removed through ICA component rejection, which causes the covariance and cross-spectral density matrices for the parametric methods to be rank-deficient, the regularization parameter λ was set to 100% in FieldTrip for all methods.

3. Statistics

The experimental design is that of a within-subject experiment; each participant was tested in all conditions. Randomization of the condition order was applied to account for order effects [50].

A cluster-based statistical analysis was performed on the source localization results of every method to answer the initial research question: is it possible to distinguish the activity of the index finger from the activity of the ring finger performing a pinch and hold force task? The research question can be formulated into a binary null-hypothesis; the two conditions (controlling using the index against using the ring fingers) are identical and the source locations and powers are drawn from the same probability distribution. To test the null hypothesis, a Monte Carlo method was applied to the grouped data from all participants; the source-space results were group-averaged per condition across all participants and the conditions were tested contrasting the perturbed against the unperturbed case per controlling finger. The p-values of the source power across all source locations was calculated and is presented in **Table 1**.

III. Results

Channel Level Analysis

The SNR was calculated on the channel level for the perturbed conditions. The channels with the highest SNR are found in the frontal region, creating a cluster around F1. This channel is highlighted with a red box in **Figure 3**. In the regular 10-10 system of EEG electrode locations, the F1 channel is positioned over the

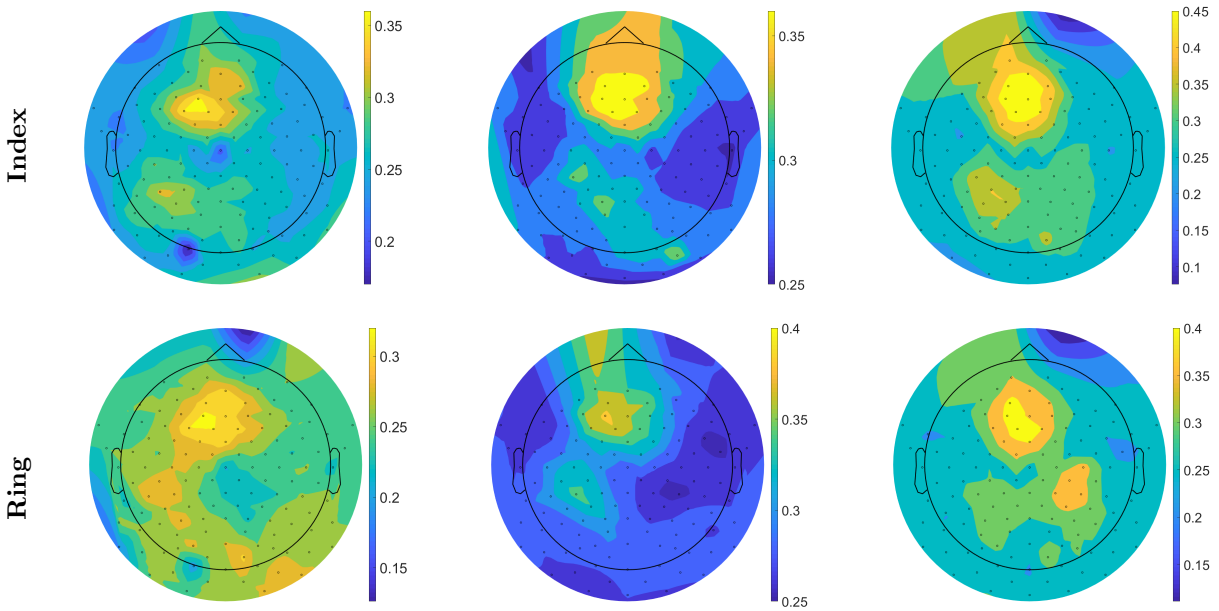

(a) *Participant #1* **(b)** *Participant #2* **(c)** *Participant #3*

Figure 5: *The signal-to-noise ratio (SNR) is plotted topographically across the head per condition for all participants. Image (a) shows the topographical plot across the 2D electrode layout for participant #1. Images (b) and (c) follow the same approach for participants #2 and #3. Images (d)-(f) present the SNR when the participants were tested using the ring finger. The positions of the electrodes are marked using dots.*

frontal cortex. F1 is examined further, as it is consistently found among the channels with the highest SNR. A second cluster of high-SNR channels is found in the left central-posterior side, around the CP3 electrode. This cluster contains the centro-parietal electrodes on the left side, which are located right above the left posterior parietal lobe. In one participant, high SNR values are also found on the right side of the head over the right posterior parietal lobe. The results of the SNR calculation are plotted separately for the index and the ring fingers in **Figure 5**.

The perturbed and unperturbed responses were compared against each other in both the time and frequency domains using the data from the F1 channel. The EEG signal was averaged per condition across all trials for each participant. The power of the signal was calculated using the multitaper frequency transformation method after averaging. There is a clear difference between the averaged signals when comparing the perturbed conditions against the unperturbed for both fingers. Differences are found mainly in the alpha and in the delta bands. There are oscillatory components in the low frequencies when the perturbations were applied. A comparison between the averaged signals recorded from the F1 channel for one participant during the perturbed and unperturbed conditions are presented on the top row in **Figure 6**. In the Appendix, an overview of the data per participant is presented in **Figures 13** and **Figure 14**.

The C3 channel is positioned over Brodmann area 4 - the primary motor cortex [51]. The position of the channel on the EEG cap is also highlighted in **Figure 3**. To investigate the involvement of the motor cortex during the experiment, the power of the signal was calculated using the same procedure as before, and the results were compared among participants for the perturbed and the unperturbed conditions. In contrast to the data from the F1 channel, there is an absence of a strong oscillatory behavior in the averaged signals. The neural oscillations during the perturbed conditions, found earlier in the alpha and in the delta bands, are almost non-distinguishable. Results from a single participant are presented on the bottom row in the **Figure 6**. An overview of the results per participant is presented in the Appendix; **Figure 15** shows the comparison between the perturbed and unperturbed conditions for the index finger and **Figure 16** for the ring finger.

Channels F1 and C3 were examined for oscillatory components in time by performing a time-frequency analysis. The C3 channel shows evidence of mu rhythm suppression, starting approximately 3 seconds before movement onset and lasting throughout the whole trial. Mu rhythm suppression is interrupted in some cases by sudden power increases during the [-1 -0.5] seconds time window. A power drop in the alpha band is also present in the data from the F1 channel. No prominent power changes relative to the baseline time window are found in the beta or gamma frequency bands. The time-frequency analysis results for all participants during the perturbed conditions are presented in **Figure 7**. All the results are presented in the Appendix in **Figures 17** and **18**.

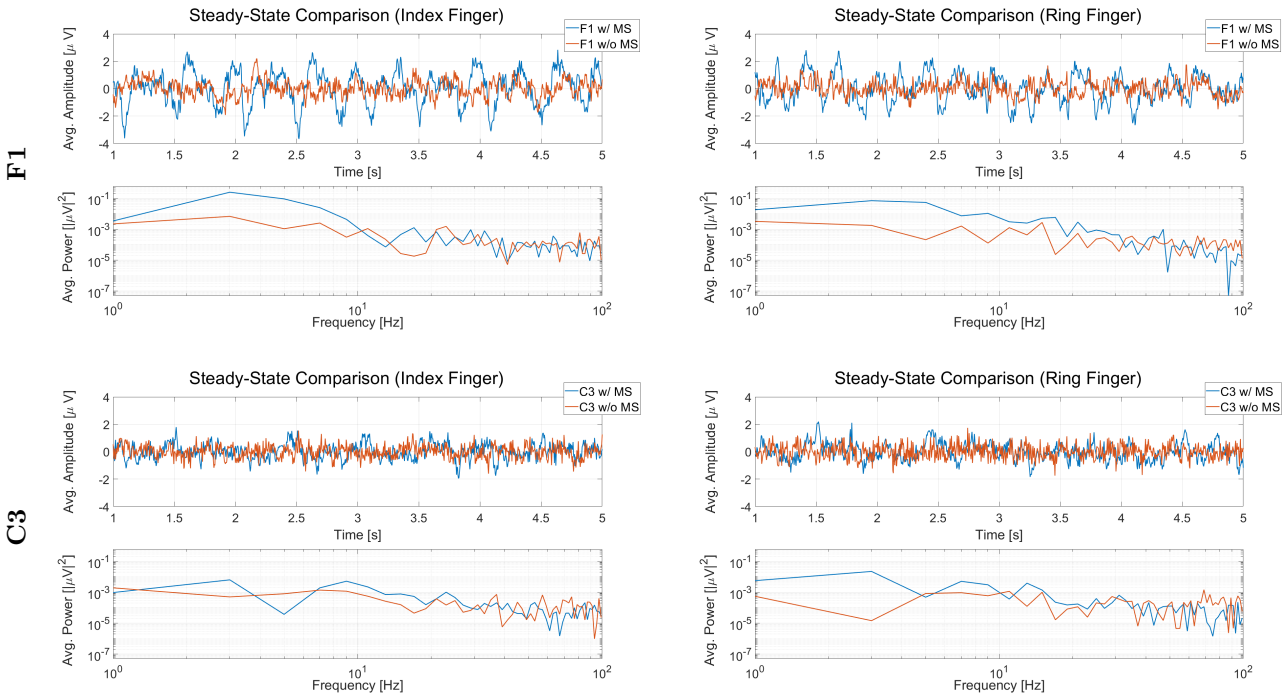

Figure 6: *The F1 and the C3 channels are analyzed separately. The timelocked signals are shown in the figures above. A comparison of the perturbed and unperturbed conditions for a single participant. The response to the perturbation is shown in blue and the unperturbed response is shown in orange. For each channel, the time-domain signals are plotted during the hold phase of the experiment, during the time window* $t_{ss} = [1\ 5]$ *seconds. The frequency power spectra of the signals are plotted below the time-domain signals.*

Source Localization

Source space results obtained using the LCMV beamformer method were averaged per condition among participants. A binary mask was used to highlight sources with power values in the 98^{th} percentile. Results are displayed in **Figure 8**. The sources with the strongest activity are biased towards the center of the head. Weak source activity is found at the motor cortex. Using this method, power is distributed across the whole brain and there are no focal sources.

In **Figure 9** the results of the DICS beamformer are shown. The previously identified power drop in the alpha band (mu rhythm suppression) was localized. The power difference was calculated by performing a frequency analysis in the pre-stimulus baseline time window $t_{bsl} = [-5\ -1]$ seconds and during the steady-state response to the perturbation in the time window $t_{ss} = [1\ 5]$ seconds, calculating the source power, and then contrasting the source power of the two individual time windows. Mu rhythm suppression is localized at both the left and right hemispheres and is present on the cortical surface and deeper inside the brain. An increase in activity is found at the posterior area of the brain, at the primary visual cortex (Brodmann area 17). Increased activity at the visual cortex is not present during the unperturbed conditions. However, there is an increase at the frontal and left parietal areas of the brain.

Using the sLORETA method, distinct clusters of strong sources are found across the brain volume. Source activity in the visual cortex is high during the perturbed conditions, similar to the results from the DICS method. Furthermore, strong activity at the left and right dorsolateral frontal cortices (Brodmann area 9) is present. Activity on the left side is focal and more pronounced. Strong sources are found at the premotor cortex (Brodmann area 6), which is stronger during the unperturbed conditions. This area is related to motor planning. Comparing the conditions with and without the perturbations we can see that the frontal sources are weaker when participants performed the motor task under the multisine perturbation.

Results from eLORETA (**Figure 11**) show activity in the same areas as sLORETA, however, the source power is lower and less focal. The power of the sources is distributed across the brain volume, with stronger activity located in the left prefrontal cortex for all cases. This activity is more pronounced in the two conditions where the perturbation was not applied.

Statistical Analysis

Source localization results for each method were statistically tested using a Monte Carlo method. We are interested in finding if there is a difference between using different fingers based on the power of the sources during the perturbed and the unperturbed conditions. Thus, the null hypothesis is binary; we calculated the probability that the two conditions are drawn from the same probability distribution. The null hypothesis

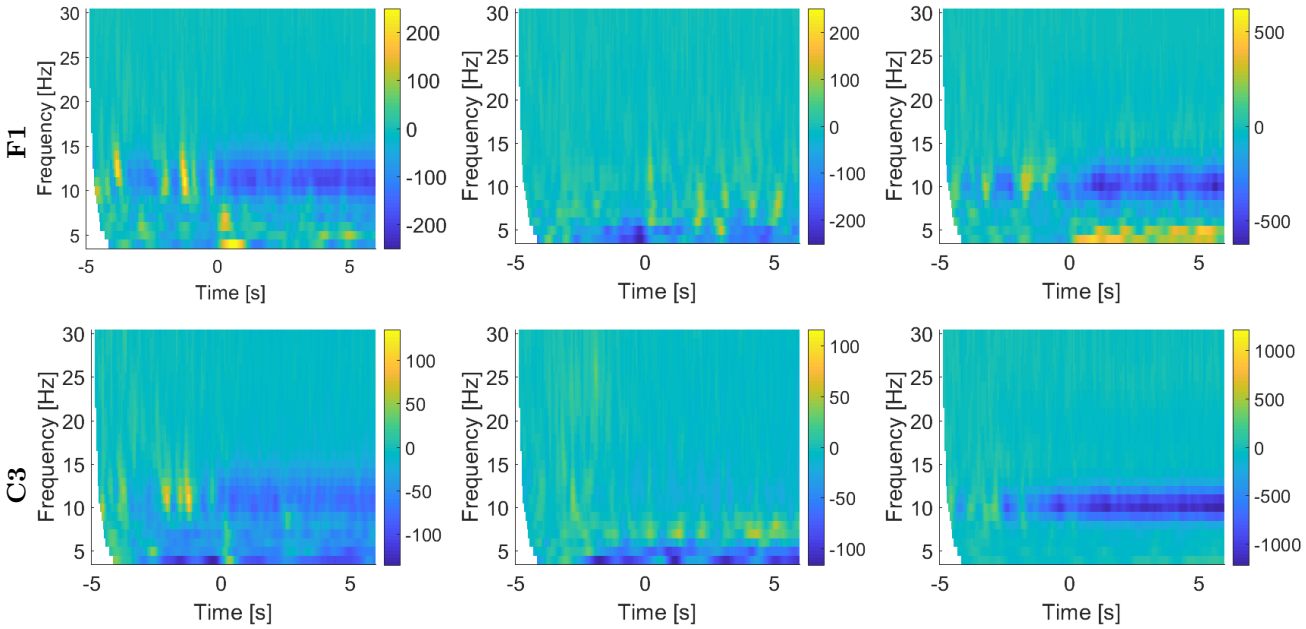

(a) *Participant #1* **(b)** *Participant #2* **(c)** *Participant #3*

Figure 7: *Time-frequency analyses of the data from the F1 and C3 channels per participant for the perturbed condition while using the index finger. Color code represents the absolute power increase or drop relative to the chosen baseline time window of [-5 -3] seconds. The power values are expressed in* $\mu V^2/Hz$.

is rejected if statistically significant p-values are found ($p < 0.05$). The differences in the results required two tests for each applied source localization method; a total of 8 tests were performed. The results are summarized in **Table 1**. Statistical significance is found and the null hypothesis is rejected only when comparing the power of the localizes sources using the DICS method between the trials performed under the position perturbation. The sources for which the p-values are statistically significant are located far away from the motor cortex. However, there are numerous sources deep in the left and right frontal cortices. This is visualized in **Figure 12**.

IV. Discussion

The goal of the present study was to examine the possibility of disentangling the activation patterns of two individual fingers - the index and the ring - during a pinch and hold force task using EEG source localization methods and position perturbations. On the channel level, strong activity in the frontal area is measured by the F1 channel. This activity is prevalent during the perturbed trials. Therefore, it may be related to motor planning, regarding the movement of the controlling finger as a response to the perturbation signal.

On the source level, the four methods provided varying results both in terms the power of the localized sources. Source localization accuracy is affected by the variability of the cranial anatomy of the subjects. Anatomical differences between the participants result in large variability in the anatomical locations of each electrode [26]. Furthermore, the farther away from the center of the head an electrode is placed, the higher the variability in terms of anatomical accuracy; this is especially important for areas close to the occipital lobe. As a result, important electrodes for source localization are possibly placed over different brain areas in different subjects. The statistical analysis performed on the source-space results indicates that separating between the two controlling fingers is not feasible using the current approach.

Channel-level

1. Time-domain analysis

The SNR of each EEG channel (**Figure 5**) was calculated for the conditions where the perturbation was applied, once per finger per participant, similarly to the literature [39, 52]. A high-SNR cluster of channels is located around F1 at the frontal area of the head. The F1 channel primarily records the activity of the supplementary motor cortex (Brodmann area 8). A second cluster is located in the area around the CP3/CP5 channels in two of the three participants. The cluster located around the CP3/CP5 channels records the activity of the postcentral gyrus, which refers to the primary somatosensory cortex (S1 - Brodmann areas 1-3) the parietal cortex, and the supramarginal gyrus (Brodmann area 40). This is a clear indication of a sensory response to the stimulus instead of active motor control as a response to the position perturbation.

The C3 channel is located closest to the left primary

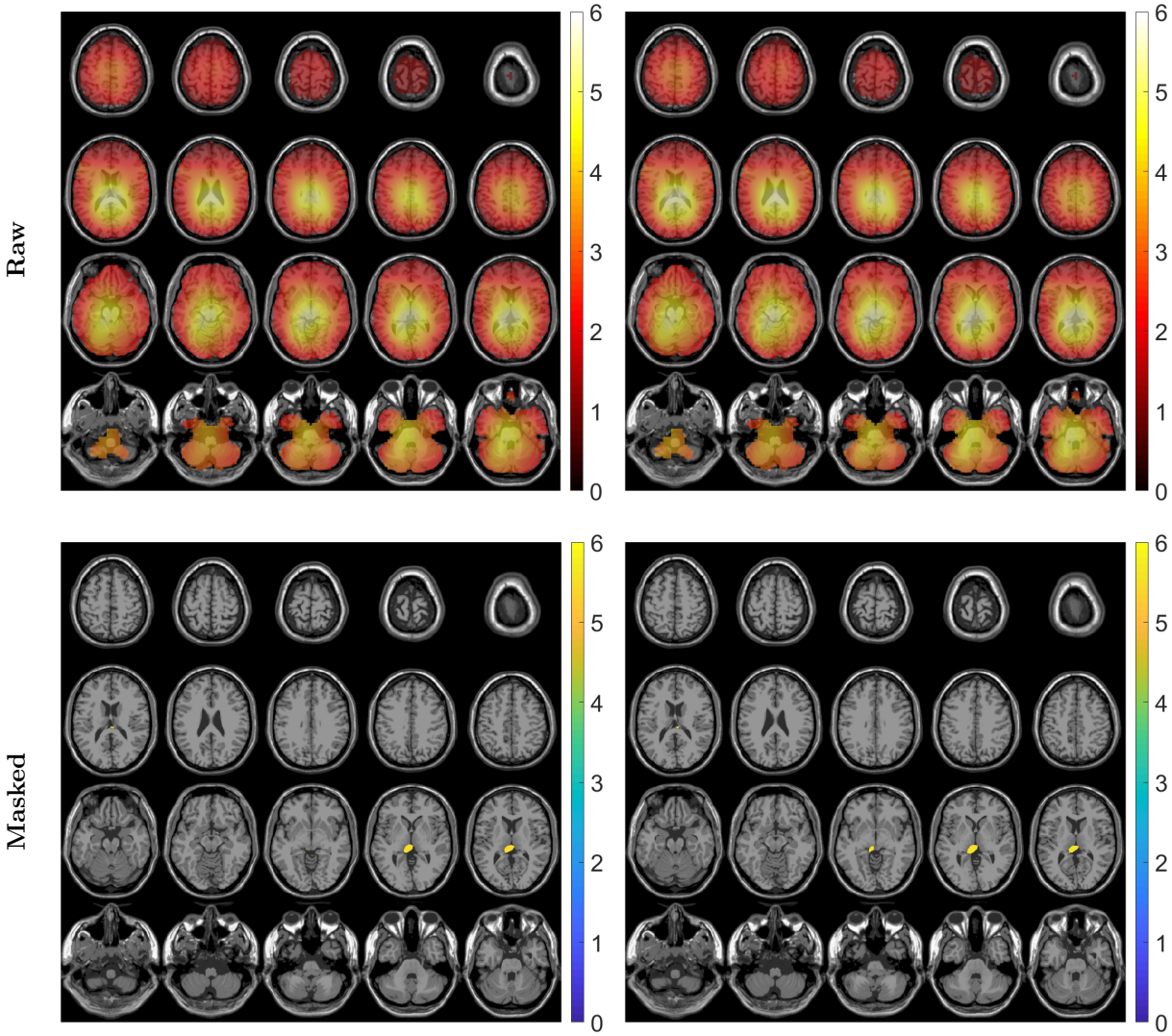

(a) *Index (MS)* **(b)** *Ring (MS)*

Figure 8: ***LCMV beamformer*** *source localization results during the perturbed conditions. The top row displays the results of the source localization, grand averaged over all participants per condition, without any applied masking. The sources with power values in the top 2% are highlighted using a binary mask and shown in the bottom row. Figures (a) and (c) show the results when participants used their index finger. Figures (b) and (d) show the results when participants used their ring finger. Each figure is accompanied by a relevant color bar. Sources with higher power values are displayed with brighter colors in both rows. The color code represents the power of the sources and is reported in a.u.*

motor cortex (M1) and is prominent in recording its activity. High-SNR activity in the C3 channel during the steady-state response to the perturbation is not found, thus the activity of the M1 is not correlated to the perturbation. This is surprising since the perturbations force the participants to correct for the changes in finger position while maintaining finger flexion; it was expected that the need to control for the perturbations would stimulate the hand area in the M1. An argument can be made that the distance between the M1 and the S1 is relatively small, thus the recorded signals could be intertwined and the second cluster represents both motor and sensory activity.

During the hold stage of the perturbed trials, the signal of the C3 channel shows low-power oscillatory behavior in the delta and alpha bands. In the literature, delta-band activity has been proposed as promising for decoding purposes, albeit with limited success [53]. Oscillations in the alpha band were investigated further; the DICS method was used to localize the sources responsible for this activity. An overview is presented in the Appendix in **Figures 16** and **15**.

The absence of oscillatory activity during the unperturbed trials is to be expected, as there is no oscillatory movement involved. The observed results are in line with this assumption.

Comparing the time-domain signals of the perturbed and the unperturbed conditions for each finger per participant shows differences which are assumed to be related to the perturbation. However, there is no

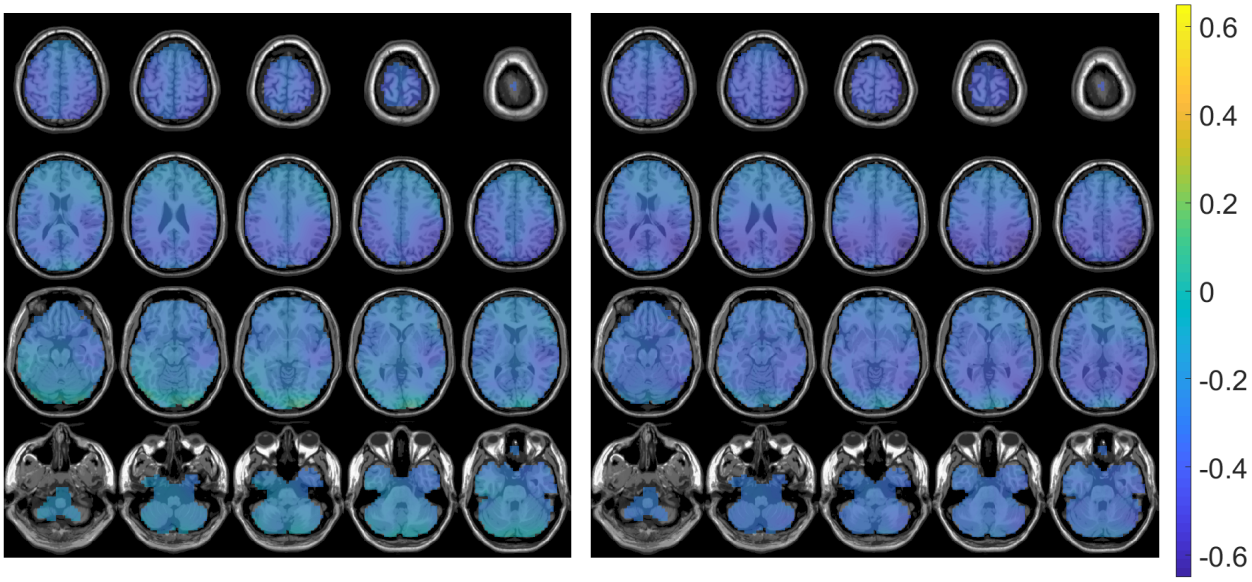

(a) *Index (MS)* **(b)** *Ring (MS)*

Figure 9: ***DICS beamformer*** *source localization results during the perturbed conditions. The sources were localized based on the power in the alpha frequency band, centered around 10 Hz with a frequency smoothing of* ± 2 *Hz. Power is normalized and contrasted between the steady-state time window* $t_{ss} = [1\ 5]$ *seconds and the pre-stimulus baseline* $t_{bsl} = [-5\ -1]$ *seconds where* $t_0 = 0$ *indicates the start of the trial. The results were grand averaged over all participants per condition, without applying any masking. Figure (a) shows the results when participants used their index finger, while (b) shows the results when participants used their ring finger. Positive values indicate a power increase relative to the baseline; similarly, negative values indicate a power drop.*

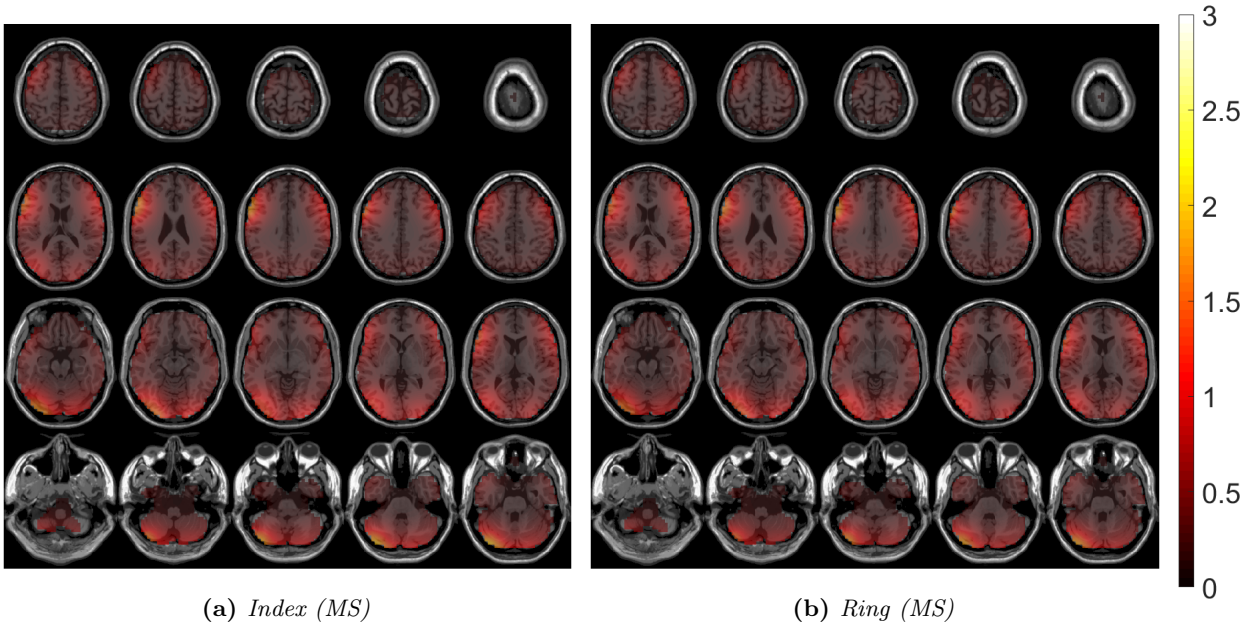

(a) *Index (MS)* **(b)** *Ring (MS)*

Figure 10: *Source localization results from the* ***sLORETA*** *method during the perturbed conditions. The sources were localized based on the time-locked EEG signals during the steady-state time window* $t_{ss} = [1\ 5]$*. The instant* $t = 0$ *indicates the start of the trial. The results were grand averaged over all participants per condition. Figure (a) shows the results when participants used the index finger. Similarly, figure (b) shows the results when participants used the ring finger. Figures are accompanied by a color bar indicating the strength of the localized sources. Highly-active sources are indicated with a brighter color. Values are reported in a.u.*

observable difference when comparing the index and the ring fingers per condition using the the SNR plots and the single-channel analysis of the F1/C3 channels. It is not possible to distinguish between the used finger for each condition using the channel-level results.

In all cases, the recorded voltages from the par-

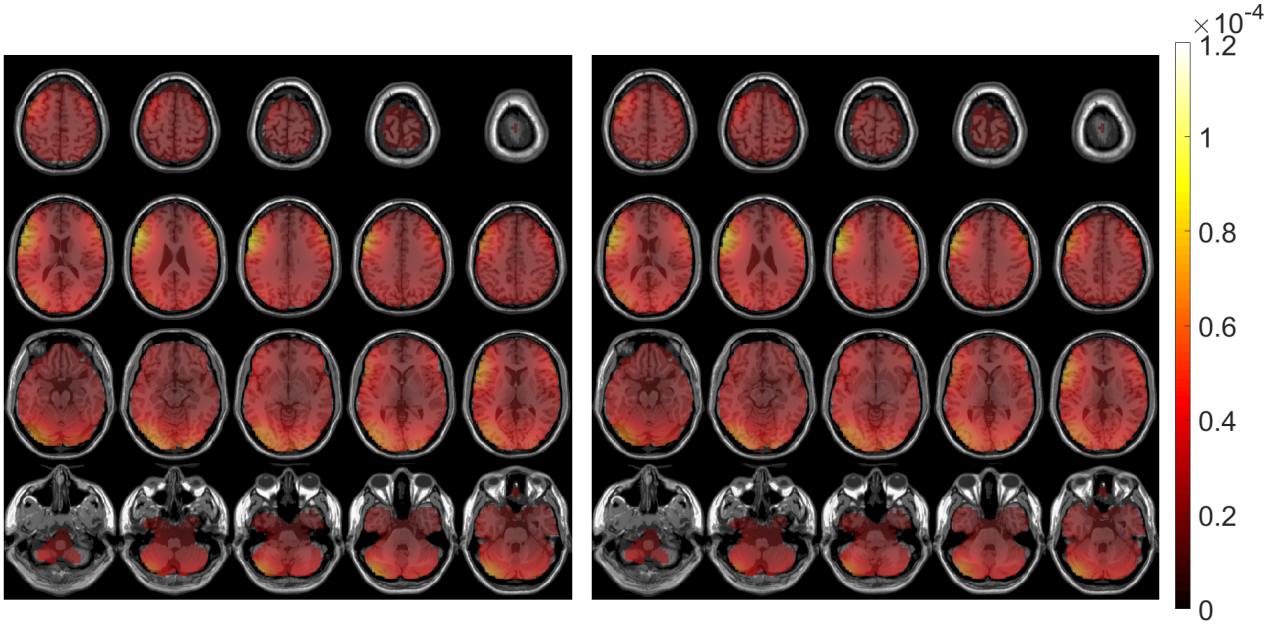

(a) *Index (MS)* **(b)** *Ring (MS)*

Figure 11: *Source localization results from the **eLORETA** method during the perturbed conditions. The sources were localized based on the time-locked EEG signals during the steady-state time window $t_{ss} = [1\ 5]$. The instant $t = 0$ indicates the start of the trial. The results were grand averaged over all participants per condition, without any applied masking. Figures (a) and (c) show the results when participants used the index finger. Similarly, figure (b) shows the results when participants used the ring finger. Figures are accompanied by a color bar indicating the strength of the localized sources. Highly-active sources are indicated with a brighter color. Values are shown in a.u.*

ticipant #3 were consistently higher. This can be attributed to using a different (larger) EEG cap for this participant. Due to the inherent physiological variability of head size and shape among participants, different cap sizes were available in the experiment, which could affect the sensitivity of the measurements, even though the impedance values per channel were checked before and after the study to be lower than 10 $k\Omega$. There is an intrinsic variability in using the EEG modality, making it difficult to use consistently for BCI applications.

2. Time-Frequency domain analysis

In the literature, beta band ERDs are reported as the most prominent effect over the motor cortex prior and during movement [21]. This power drop in the beta band (14-30 Hz) is initiated approximately 500 ms before movement onset and is followed by an increase in power at the post-movement execution time window. We performed a time-frequency analysis on the EEG signals from the F1 and C3 channels to locate the beta ERD. An absence of strong neural oscillations in the beta band is observed in our findings. It is possible that the lack of a prominent beta band oscillation is due to the design of the experiment; motor preparation and thus the beta band ERD could have occurred during the baseline time window, thus not showing a clear decrease in power during the execution of the motor task. One possible adjustment to the experimental design could be the removal of the 3-second countdown timer, leaving less time for the participants to prepare for the task ahead. Using an earlier time period as a baseline is also possible, however this approach creates other issues, such as longer times between trials and thus longer experimentation times.

A prominent ERD is found at the alpha band (8-12 Hz), centered around 11 Hz. This neural activity is the mu rhythm. Mu rhythms occur in the sensorimotor cortex and are associated with coordinating perception and voluntary movement [40]. Mu rhythm suppression is reported when a person performs a motor action or an imaginary motor action with sufficient training. As a result, these power drops are used to design motor BCIs [10, 54]. What is interesting, however, is that the ERD at the alpha band is observable in both the F1 and C3 electrodes for both the perturbed and unperturbed conditions. This is visible in participants #1 and #3 during the motor preparation stage during the time window of [-3 0] seconds. For participant #2, this ERD is non-detectable. This could also be attributed to possible motor preparation and imaginary movements occurring during the baseline time window, as reported earlier. Alpha band decoding strategies exploiting mu rhythm suppression have been used in the literature with mixed results [55, 56].

Two participants also exhibit short high power

		MS	NP
LCMV	min(p)	0.2517	1
	max(p)	1	1
	mean(p)	0.9722	1
	sum($p < 0.05$)	0	0
DICS	min(p)	$\approx 10^{-3}$	1
	max(p)	1	1
	mean(p)	0.8076	1
	sum($p < 0.05$)	26593	0
sLORETA	min(p)	0.1359	1
	max(p)	1	1
	mean(p)	0.9872	1
	sum($p < 0.05$)	0	0
eLORETA	min(p)	0.1309	1
	max(p)	1	1
	mean(p)	0.9693	1
	sum($p < 0.05$)	0	0

Table 1: *Results of the Monte Carlo cluster-based permutation test. The results are reported per source localization method and condition. The results of the statistical test between the two conditions with an applied multisine position perturbation are reported in the column titled "MS". The column titled "NP" stands for "no-perturbation" and indicates the conditions without a position perturbation. The minimum and maximum p-values are reported for each case, as well as the mean of the distribution and the number of p-values indicating statistical significance.*

bursts in the alpha band right after the countdown stimulus is visually presented. These bursts are detected for both the F1 and the C3 channels. This is a strange behavior which can be attributed to minor movements during the preparation stage, such as pushing against the lever followed by relaxing the fingers. Approximately 500 ms before the trial starts we can see these high-power bursts giving way to the mu rhythm suppression, which persists throughout the whole trial.

Finger kinematics have been decoded in the literature from the delta band ($f_d \leq 4$ Hz) during repetitive finger movements [53]. Delta-band signals are considered favorable for decoding finger movements, as they can have more power and are less likely to be corrupted by muscular artifacts and noise [57]. Contreras-Vidal et al. report in their work that the results varied greatly among participants, while poor to moderate decoding accuracies are reported. They conclude that kinematics can be inferred by employing genetic algorithms and linear decoders, to some extent. Our time-frequency analysis demonstrates that this low-frequency activity is inconsistent among participants; for participant #1 there is a burst of high-power activity centered around the experiment onset time point t_0. Participant #2 exhibits an erratic delta-band activity, with bursts of power later during the trials. Finally, participant #3 exhibits an increase in power that is

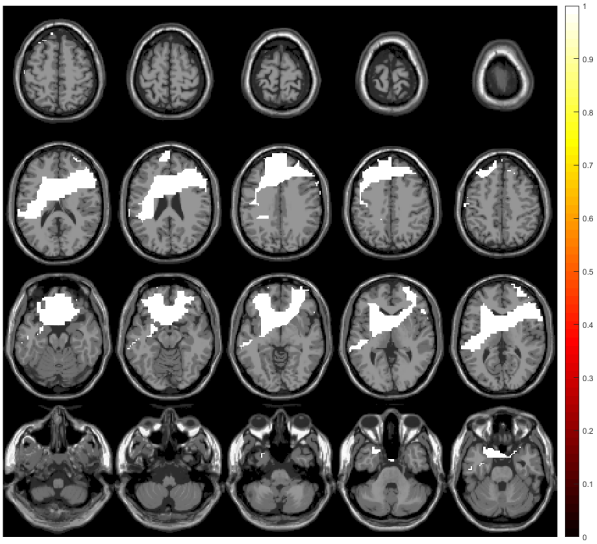

Figure 12: *The figure depicts the location of the sources for which statistical significance ($p \leq 0.05$) is calculated using the results from the DICS source localization method.*

sustained throughout the complete trial. As a result, we decided not to focus on the delta frequency band in the current work.

Source-space results

Differences between neural responses found on the channel-space indicate differences also present on the source-space; however, the opposite assumption cannot be made due to the nature of the inverse problem, the choice of source localization method, and the forward model used. As such, similar channel-level responses do not guarantee that there are no differences on the source space.

Four of the most prominent methods in the literature were selected to perform source localization in time and in frequency domain and evaluate the results in terms of accuracy and consistency. Each method gave varying results in terms of source power. The most important parameters affecting source localization results are the choice of forward model [9], the number of tissue layers [35], the anisotropy of each tissue [8], the tissue conductivity values [58], the produced lead field matrix [36], the source localization method used [6], and in many cases the choice of the regularization parameter λ [44, 45].

A common spatial filter was constructed and used to obtain the source-space results using beamforming. The use of a common spatial filter per participant across all conditions guaranteed that the results would be directly comparable. These filters provide numerous benefits, such as higher fidelity due to the incorporation of more information from multiple conditions, since the covariance and cross-spectral density matrices are based on the combined datasets [27]. They also allow us to compare the results directly, as they

eliminate the contribution of the filter to the localized sources. As a result, any differences in the source level results can be attributed to differences in the actual sources instead of filter differences and errors.

For the LCMV beamformer, the localized sources were grouped at the center of the head. There is minimal activity in the M1 area of the head, as depicted in **Figure 8**. This was unexpected, as the lead fields were normalized and we also calculated and reported the NAI to correct for the depth bias. Even so, the sources with the highest power were consistently localized in the center of the head across all conditions. In the literature, fMRI results have been shown to produce similar results [59]. Results from an fMRI motor task have shown activity in the center of the head during a finger flexion task. However, in that study, activity has been also found in the M1 area and the supplementary motor cortex (SMA). However, in that study, participants were performing finger flexion periodically, every 2 seconds. This would be equivalent to examining the ERP centered around the t_0 mark of the trial initiation instead of a pinch and hold task like in our study. Using LCMV, there are no visible differences between the cortical activity of the participants when using different fingers to perform the control task. This holds true for both the perturbed and the unperturbed conditions.

The sources responsible for the mu rhythm suppression were localized using the DICS beamformer. Localization using this method requires a different approach: instead of calculating the NAI as before, we contrasted the activity during the steady-state time window to a baseline window of equal length. A power reduction in the M1/S1 area is found, yet not as strong or focal as initially expected. These power drops are also seen in both the left and right hemispheres. A possible explanation for this is that mu rhythm suppression can occur through both realized and imaginary movements. Mu rhythm activity relates to the mirror neuron system, linking perception to motor action [60]. Similarly to the LCMV method, the results obtained using DICS are visually indistinguishable when comparing between using the index and the ring fingers for the perturbed and the unperturbed conditions.

Two non-parametric methods were also used; sLORETA and eLORETA. The two methods provided similar results in terms of the location of the sources, but the sources differed in terms of their power. Similarly to the DICS method, the results show strong activity in the visual cortex during the perturbed trials and stronger activity in the prefrontal cortex during the unperturbed trials. Sources with high power in the hand area of the M1 were not found; this indicates that the cortical contribution when maintaining a constant pinching force during a hold task when using individual fingers is very small and can not be detected using EEG source localization.

The validity of the results is confirmed by reviewing the power of the localized source in the posterior side of the head, the visual cortex. The left side of the posterior (visual) cortex shows higher activation during the perturbed conditions; this is expected since the haptic manipulator was placed on the right side of the visual field of the participants. The 15 Hz movement of the device was registered by the left visual cortex. The absence of such activity in the unperturbed trials is also to be expected.

Beamforming techniques provided inconsistent results compared to the sLORETA and eLORETA methods. The latter produced more focal sources, as expected from the literature [21]. There are no visual differences between the source locations or their power to indicate it is possible to separate between the index and the ring fingers using the above methods.

Statistical analysis

The cluster-based permutation test, performed on the source-space results from each method, did not reveal a difference between the use of the index finger and the ring finger in the operation of the haptic manipulator for neither the perturbed nor the unperturbed conditions for three out of four methods. For the DICS method, when comparing the source-space data from the perturbed conditions, the cluster-based permutation test revealed a significant difference between the use of the index finger and the ring finger in the operation of the haptic manipulator ($p < 0.05$). However, this effect is most pronounced in the sources located deep in the frontal cortex; this may have been caused due to noise or background brain activity in the alpha band and thus be a false positive. We do not have a reason to believe this is a true positive, thus validating the use of the DICS method in the context of the current study. Furthermore, the statistical analysis of the sLORETA and the eLORETA methods indicate it is not possible to distinguish between the used finger from the source space during the hold phase of the movement using non-parametric methods.

Kuo et al. performed a similar study on EEG source localization of finger movements. In their study, they did not separate between two fingers, but they managed to consistently localize the movement of the thumb on the hand area in the M1 using the sLORETA method [21]. They report that they used twice as many EEG channels in their study and subject-specific head models, derived through MRI. Their results were also compared against BOLD responses from fMRI during the same motor tasks. It may be possible to achieve better results in the future by increasing the accuracy of the forward model by making it subject-specific; however, this increases the cost of the study and requires more time. Our results do not encourage this approach.

Limitations

Forward model errors

The quality of the inverse solutions is affected by the accuracy of the forward model. The effects of the parameters of the forward model on the inverse solutions have been reviewed in the literature [36]. In the present study, a three-layer BEM head model, constructed from a template MRI, was used. Template BEM head models increase localization errors across the brain regions which deviate from the true geometry. This is valid for both three and four-layer models. BEM head models are homogeneous and the three-layered variant does not model the cerebrospinal fluid (CSF). Four-layer models produce more accurate results, demonstrating the importance of including the CSF layer in a model [9]. However, advanced imaging and segmentation methods are required to model the CSF layer.

In BEM, the assumption of homogeneity and lack of anisotropy in different tissues of the same layer is necessary, yet inaccurate [46]. The anisotropic properties of the skull tissue, as well as the white matter, are ignored [61]. Finite element methods (FEM) allow for the construction of a realistic head model which accounts for the anisotropic propertes of each tissue, thus improving the results of the inverse solution. These numerical models are more complex and computationally demanding than analytical models, however, they offer higher resolution and localization accuracy [5]. Constructing such a model requires a patient-specific MRI. MRI-extracted information is preferable to template head models for higher accuracy [62]. However, in the present study, it was not possible to obtain such data from the participants due to the added cost and required resources.

When constructing a homogeneous head model, the conductivity values of the layers must be selected. The skull tissue is inherently anisotropic, as it consists of two hard outer layers enclosing a spongious inner layer. Its conductivity is argued to be patient-specific and the conductivity of the skull plays an important role in the accuracy of the simulation results [36]. Brain tissue also exhibits anisotropic properties. Gray matter is considered homogeneous and isotropic, whereas white matter is much more anisotropic and inhomogeneous in comparison [63]. Thus, the gray matter, the scalp, and the cerebrospinal fluid (CSF) are assumed to have isotropic conductive properties when constructing a realistic head model [61]. In the present study, the conductivity values were selected according to the literature; it is argued that the ratio between the skull and scalp tissues is more important than the individual conductivities [35]. These values have been presented in **Figure 4**.

The incorporation of prior information in a realistic head model also improves the accuracy of the localized sources. In the literature, solving the inverse problem using EEG source localization methods during a finger movement task using a FEM head model, shows a high spatial correlation between the localized sources and fMRI activation sites [59]. This indicates that a complex numerical head model with the incorporation of prior information concerning the location of the sources, obtained through fMRI, can reduce localization errors and increase the accuracy of the inverse solutions. The reduction of localization errors can be attributed to the elimination of discrepancies between the conducting brain model and the true head physiology. Constructing more complex head models improves the spatial accuracy of the inverse solutions, it requires, however, more resources and more intricate calculations need to be completed when solving the inverse problem. Thus is not ideal for BCI applications where real-time processing plays an important role.

Inverse solutions

Regularization plays an important role in the accuracy of the inverse solutions. The regularization parameter introduces noise in the covariance matrix (in the LCMV case) and the cross-spectral density matrix (in the DICS case), which makes the matrices full-rank and allows for the computation of the inverse solution. Performing ICA decomposition and rejecting components to remove artifacts lowers the rank of these matrices [29, 31]. Using ICA to reject EOG artifacts reduces the rank of the matrix, and thus the regularization parameter is set to $\lambda = 1$ in FieldTrip. For instance, in the case of the LCMV, using a smaller regularization parameter the sources are spread out in the edges of the brain, changing the overall source estimation dramatically. However, estimating the regularization parameter is a complex task that has been reviewed extensively in the literature [6].

Beamformers localize one dipole source at a time by isolating contributions from non-relevant current sources. This is accomplished by constructing spatial filters according to the given source model. As a result, beamformers are sensitive to noise, as it is hard to construct accurate spatial filters to zero out the contribution of spontaneous source power changes, making them more suitable for MEG data [64]. Higher-density source models might lead to worse localization results when beamforming approaches are used in EEG. Furthermore, brain activity is rarely focal in nature. In many cases, sources in the brain are correlated in their activity [46]. Beamformers have been shown to perform poorly when correlated sources are present at a given time instance [65]. This might explain the reason why stronger sources are found in the center of the brain instead of the M1 using the LCMV method.

The two non-parametric methods offer more focal solutions at a faster computational speed. However, they did not manage to find high-power sources in the M1. Source locations are consistent between the methods, indicating that a strong cortical effect in the M1 is not present during a steady pinch and hold task. The goal of the current study was to examine the

possibility of discerning between using two different fingers under perturbed and unperturbed motor tasks; the physiological accuracy of the source localization methods, while not of direct importance, still plays a significant role in identifying the relevant activity in the brain. The results of the statistical analysis have shown that the source space activity of the two fingers, using the methods explained in the present study, is very similar.

Other limitations

In the case of EEG source localization, it is important to use artifact-free data. Cleaning EEG data is an interactive process, as trials can be contaminated by EMG or other artifacts. During the analysis, visual inspection of the data proved to be more accurate in rejecting noisy trials. Furthermore, some artifacts are introduced through common activities such as eye blinks. To make a robust system that can be used in BCI, these artifacts are best dealt with through ICA and component rejection. While in offline data processing ICA can be used without any downsides to analyze EEG data, this is not possible for real-time applications. ICA decomposition is a time-consuming process that requires minutes to analyze a few seconds of data, which introduces delays and increases the latency between command and execution. In the present study, the data were recorded and analyzed offline, thus ICA was employed during cleaning the EEG data; this is a luxury that is not available during real-time data processing for BCI. Furthermore, the inherent variability of ICA can affect EEG signals even when removing EOG artifacts. Algorithms have been developed to improve the performance of component rejection without human supervision, however, it is still advised to visually inspect and individually decide which components should be rejected when cleaning EEG data [31].

V. Conclusions

- Parametric methods (sLORETA and eLORETA) were computationally efficient and provided more focal sources when compared to parametric (LCMV and DICS beamformers).
- Active sources during the hold phase of the experiment are found in the frontal cortex and the visual cortex. The former are close to the supplementary motor area (Brodmann area 8) and could be related to motor planning.
- No source activity in the hand areas of the M1/S1 during the hold phase of the motor task (time window $t_{ss} = [1\ 5]$ seconds).
- The statistical analysis of the source-space results indicates that the two fingers have very similar cortical responses. Using the methods of the present study, no statistically significant sources were found.
- Research using subject-specific realistic head models, constructed using individualized MRI scans, which also take into account tissue anisotropy using FEM, could provide different results.

References

[1] M. Modaneszadeh, R. N. Schmidt, C. Medical, and C. Avenue, "Wireless , 32-Channel9 Eeg and Epilepsy Monitoring System," *Instrumentation*, vol. 1157, no. C, pp. 1157–1160, 1997.

[2] A. A. Gaho, S. Hyder, and A. Musavi, "EEG Signals based Brain Source Localization Approaches," vol. 9, no. 9, pp. 253–261, 2018.

[3] P. H. Schimpf, C. Ramon, and J. Haueisen, "Dipole models for the EEG and MEG," *IEEE Transactions on Biomedical Engineering*, vol. 49, no. 5, pp. 409–418, 2002.

[4] J. C. de Munck, B. W. van Dijk, and H. Spekreijse, "Mathematical dipoles are adequate to describe realistic generators of human brain activity.," *IEEE transactions on bio-medical engineering*, vol. 35, pp. 960–6, nov 1988.

[5] M. A. Jatoi and N. Kamel, *Brain Source Localization Using EEG Signal Analysis*, vol. 91. 2017.

[6] R. Grech, T. Cassar, J. Muscat, K. P. Camilleri, S. G. Fabri, M. Zervakis, P. Xanthopoulos, V. Sakkalis, and B. Vanrumste, "Review on solving the inverse problem in EEG source analysis," *Journal of NeuroEngineering and Rehabilitation*, vol. 5, pp. 1–33, 2008.

[7] C. J. Stok, "The influence of model parameters on EEG/MEG single dipole source estimation," *IEEE Transactions on Biomedical Engineering*, vol. BME-34, pp. 289–296, apr 1987.

[8] C. Ramon, P. H. Schimpf, and J. Haueisen, "Influence of head models on EEG simulations and inverse source localizations," *BioMedical Engineering Online*, vol. 5, pp. 1–13, 2006.

[9] Z. Akalin Acar and S. Makeig, "Effects of forward model errors on EEG source localization," *Brain Topography*, vol. 26, no. 3, pp. 378–396, 2013.

[10] S. Machado, F. Araújo, F. Paes, B. Velasques, M. Cunha, H. Budde, L. F. Basile, R. Anghinah, O. Arias-Carrión, M. Cagy, R. Piedade, T. A. De Graaf, A. T. Sack, and P. Ribeiro, "EEG-based brain-computer interfaces: An overview of basic concepts and clinical applications in neurorehabilitation," *Reviews in the Neurosciences*, vol. 21, no. 6, pp. 451–468, 2010.

[11] M. G. Bleichner, Z. V. Freudenburg, J. M. Jansma, E. J. Aarnoutse, M. J. Vansteensel, and N. F. Ramsey, "Give me a sign: decoding four

complex hand gestures based on high-density ECoG," *Brain Structure and Function*, vol. 221, no. 1, pp. 203–216, 2016.

[12] M. G. Wentrup, K. Gramann, E. Wascher, and M. Buss, "EEG source localization for brain-computer-interfaces," *2nd International IEEE EMBS Conference on Neural Engineering*, vol. 2005, pp. 128–131, 2005.

[13] N. Birbaumer, "Breaking the silence: Brain-computer interfaces (BCI) for communication and motor control," *Psychophysiology*, vol. 43, no. 6, pp. 517–532, 2006.

[14] J. M. Carmena, "Advances in Neuroprosthetic Learning and Control," *PLOS Biology*, vol. 11, p. e1001561, may 2013.

[15] A. L. Benabid, T. Costecalde, A. Eliseyev, G. Charvet, A. Verney, S. Karakas, M. Foerster, A. Lambert, B. Morinière, N. Abroug, M. C. Schaeffer, A. Moly, F. Sauter-Starace, D. Ratel, C. Moro, N. Torres-Martinez, L. Langar, M. Oddoux, M. Polosan, S. Pezzani, V. Auboiroux, T. Aksenova, C. Mestais, and S. Chabardes, "An exoskeleton controlled by an epidural wireless brain–machine interface in a tetraplegic patient: a proof-of-concept demonstration," *The Lancet Neurology*, vol. 18, no. 12, pp. 1112–1122, 2019.

[16] R. Grave De Peralta Menendez, M. M. Murray, C. M. Michel, R. Martuzzi, and S. L. Gonzalez Andino, "Electrical neuroimaging based on biophysical constraints," *NeuroImage*, vol. 21, no. 2, pp. 527–539, 2004.

[17] G. Pfurtscheller and C. Neuper, "Motor imagery and direct brain-computer communication," *Proceedings of the IEEE*, vol. 89, no. 7, pp. 1123–1134, 2001.

[18] V. S. Handiru, A. P. Vinod, and C. Guan, "EEG Source Imaging of Movement Decoding," *IEEE Syst. Man, Cybern. Mag.*, vol. 4, pp. 14–23, 2018.

[19] W. Schellekens, N. Petridou, and N. F. Ramsey, "Detailed somatotopy in primary motor and somatosensory cortex revealed by Gaussian population receptive fields," *NeuroImage*, vol. 179, no. May, pp. 337–347, 2018.

[20] A. Chaudhuri and A. Routray, "Source imaging of simple finger movements captured during auditory response tasks using space-time-frequency based sparsity constraints," in *2016 38th Annual International Conference of the IEEE Engineering in Medicine and Biology Society (EMBC)*, vol. 57, pp. 4087–4092, IEEE, aug 2016.

[21] C. C. Kuo, P. Luu, K. K. Morgan, M. Dow, C. Davey, J. Song, A. D. Malony, and D. M. Tucker, "Localizing movement-related primary sensorimotor cortices with multi-band EEG frequency changes and functional MRI," *PLoS ONE*, vol. 9, no. 11, 2014.

[22] G. Pfurtscheller and F. H. Lopes Da Silva, "Event-related EEG/MEG synchronization and desynchronization: Basic principles," *Clinical Neurophysiology*, vol. 110, no. 11, pp. 1842–1857, 1999.

[23] G. Christiansson, *Hard master, soft slave haptic teleoperation*. 2007.

[24] A. D. Astin, "Finger force capability: measurement and prediction using anthropometric and myoelectric measures," pp. 1–103, 1999.

[25] R. Pintelon and J. Schoukens, *System Identification: A Frequency Domain Approach, Second Edition*. Hoboken, NJ, USA: John Wiley & Sons, Inc., 2nd ed., mar 2012.

[26] R. Oostenveld and P. Praamstra, "The five percent electrode system for high-resolution EEG and ERP measurements," *Clinical Neurophysiology*, vol. 112, no. 4, pp. 713–719, 2001.

[27] R. Oostenveld, P. Fries, E. Maris, and J. M. Schoffelen, "FieldTrip: Open source software for advanced analysis of MEG, EEG, and invasive electrophysiological data," *Computational Intelligence and Neuroscience*, vol. 2011, 2011.

[28] A. Delorme and S. Makeig, "EEGLAB: An open source toolbox for analysis of single-trial EEG dynamics including independent component analysis," *Journal of Neuroscience Methods*, vol. 134, no. 1, pp. 9–21, 2004.

[29] M. Ungureanu, C. Bigan, R. Strungaru, and V. Laarescu, "Independent Component Analysis Applied in Biomedical Signal Processing," *Journal of the Institute of Measurement Science SAS*, vol. 4, no. 2, pp. 1–8, 2004.

[30] E. D. Farahani, J. Wouters, and A. van Wieringen, "Contributions of non-primary cortical sources to auditory temporal processing," *NeuroImage*, vol. 191, no. December 2018, pp. 303–314, 2019.

[31] M. B. Pontifex, K. L. Gwizdala, A. C. Parks, M. Billinger, and C. Brunner, "Variability of ICA decomposition may impact EEG signals when used to remove eyeblink artifacts," *Psychophysiology*, vol. 54, no. 3, pp. 386–398, 2017.

[32] A. de Cheveigné and D. Arzounian, "Robust detrending, rereferencing, outlier detection, and inpainting for multichannel data," *NeuroImage*, vol. 172, no. February, pp. 903–912, 2018.

[33] R. Oostenveld, D. F. Stegeman, P. Praamstra, and A. Van Oosterom, "Brain symmetry and topographic analysis of lateralized event-related potentials," *Clinical Neurophysiology*, vol. 114, no. 7, pp. 1194–1202, 2003.

[34] C. J. Holmes, R. Hoge, L. Collins, R. Woods, A. W. Toga, and A. C. Evans, "Enhancement of MR Images Using Registration for Signal Averaging," *Journal of Computer Assisted Tomography*, vol. 22, pp. 324–333, mar 1998.

[35] S. Vallaghé and M. Clerc, "A global sensitivity analysis of three- and four-layer EEG conductivity models.," *IEEE transactions on bio-medical engineering*, vol. 56, pp. 988–95, apr 2009.

[36] H. Hallez, B. Vanrumste, R. Grech, J. Muscat, W. De Clercq, A. Vergult, Y. D'Asseler, K. P. Camilleri, S. G. Fabri, S. Van Huffel, and I. Lemahieu, "Review on solving the forward problem in EEG source analysis," *Journal of Neuro-Engineering and Rehabilitation*, vol. 4, 2007.

[37] Z. Zhang, "Iterative point matching for registration of free-form curves and surfaces," *International Journal of Computer Vision*, vol. 13, no. 2, pp. 119–152, 1994.

[38] P. Besl and N. D. McKay, "A method for registration of 3-D shapes," *IEEE Transactions on Pattern Analysis and Machine Intelligence*, vol. 14, pp. 239–256, feb 1992.

[39] M. P. Vlaar, T. Solis-Escalante, A. N. Vardy, F. C. Van Der Helm, and A. C. Schouten, "Quantifying nonlinear contributions to cortical responses evoked by continuous wrist manipulation," *IEEE Transactions on Neural Systems and Rehabilitation Engineering*, vol. 25, no. 5, pp. 481–491, 2017.

[40] D. L. Schomer and F. L. da Silva, *Niedermeyer's Electroencephalography: Basic Principles, Clinical Applications, and Related Fields*. LWW, 2010.

[41] B. D. Van Veen, W. Van Drongelen, M. Yuchtman, and A. Suzuki, "Localization of brain electrical activity via linearly constrained minimum variance spatial filtering," *IEEE Transactions on Biomedical Engineering*, vol. 44, no. 9, pp. 867–880, 1997.

[42] J. Gross, J. Kujala, M. Hämäläinen, L. Timmermann, A. Schnitzler, and R. Salmelin, "Dynamic imaging of coherent sources: Studying neural interactions in the human brain," *Proceedings of the National Academy of Sciences of the United States of America*, vol. 98, no. 2, pp. 694–699, 2001.

[43] P.-M. RD, M. CM, and L. D, "Low resolution electromagnetic tomography: a new method for localizing electrical activity in the brain.," *International Journal of Psychophysiology*, vol. 18, no. 94, pp. 49–65, 1994.

[44] Pascual-Marqui R D, "Standardized low resolution brain electromagnetic tomography (sLORETA): technical details," *Methods & Findings in Experimental & Clinical Pharmacology*, vol. 24, pp. 5–12, 2002.

[45] R. D. Pascual-Marqui, "Discrete, 3D distributed, linear imaging methods of electric neuronal activity. Part 1: exact, zero error localization," pp. 1–16, 2007.

[46] S. Baillet, J. C. Mosher, and R. M. Leahy, "Electromagnetic brain mapping," *IEEE Signal Processing Magazine*, vol. 18, no. 6, pp. 14–30, 2001.

[47] Muthuraman, H. Hellriegel, N. Hoogenboom, A. R. Anwar, K. G. Mideksa, H. Krause, A. Schnitzler, G. Deuschl, and J. Raethjen, "Beamformer source analysis and connectivity on concurrent EEG and MEG data during voluntary movements," *PLoS ONE*, vol. 9, no. 3, 2014.

[48] S. Baillet, "Toward functional imaging of cortical electrophysiology markovian models for the source estimation of magneto/electroencephalography and experimental assessments.," 1998.

[49] Y. Jonmohamadi, G. Poudel, C. Innes, and R. Jones, "Source-space ICA for EEG source separation, localization, and time-course reconstruction," *NeuroImage*, vol. 101, pp. 720–737, 2014.

[50] J. de Winter and D. Dodou, *Human subject research for engineers: A practical guide*. 2017.

[51] E. N. Marieb and K. Hoehn, *Human Anatomy & Physiology*. Pearson, 11th ed., 2018.

[52] M. P. Vlaar, G. Birpoutsoukis, J. Lataire, M. Schoukens, A. C. Schouten, J. Schoukens, and F. C. Van Der Helm, "Modeling the Nonlinear Cortical Response in EEG Evoked by Wrist Joint Manipulation," *IEEE Transactions on Neural Systems and Rehabilitation Engineering*, vol. 26, no. 1, pp. 205–215, 2018.

[53] A. Y. Paek, H. A. Agashe, and J. L. Contreras-Vidal, "Decoding repetitive finger movements with brain activity acquired via non-invasive electroencephalography," *Frontiers in Neuroengineering*, vol. 7, no. MAR, pp. 1–18, 2014.

[54] E. C. Leuthardt, G. Schalk, J. Roland, A. Rouse, and D. W. Moran, "Evolution of brain-computer interfaces: Going beyond classic motor physiology," *Neurosurgical Focus*, vol. 27, no. 1, pp. 4–7, 2009.

[55] B. Blankertz, C. Sannelli, S. Halder, E. M. Hammer, A. Kübler, K.-R. Müller, G. Curio, and T. Dickhaus, "Neurophysiological predictor of SMR-based BCI performance," *NeuroImage*, vol. 51, pp. 1303–1309, jul 2010.

[56] M. K. Hazrati and A. Erfanian, "An online EEG-based brain–computer interface for controlling hand grasp using an adaptive probabilistic neural network," *Medical Engineering & Physics*, vol. 32, pp. 730–739, sep 2010.

[57] I. I. Goncharova, D. J. McFarland, T. M. Vaughan, and J. R. Wolpaw, "EMG contamination of EEG: Spectral and topographical characteristics," *Clinical Neurophysiology*, vol. 114, no. 9, pp. 1580–1593, 2003.

[58] N. Chauveau, X. Franceries, B. Doyon, B. Rigaud, J. P. Morucci, and P. Celsis, "Effects of skull thickness, anisotropy, and inhomogeneity on forward EEG/ERP computations using a spherical three-dimensional resistor mesh model.," *Human brain mapping*, vol. 21, pp. 86–97, feb 2004.

[59] T. S. Kim, Y. Zhou, S. Kim, and M. Singh, "EEG distributed source imaging with a realistic finite-element head model," *IEEE Transactions on Nuclear Science*, vol. 49 I, no. 3, pp. 745–752, 2002.

[60] J. A. Pineda, "The functional significance of mu rhythms: Translating "seeing" and "hearing" into "doing"," *Brain Research Reviews*, vol. 50, no. 1, pp. 57–68, 2005.

[61] Z. J. Koles, "Trends in EEG source localization," *Electroencephalography and Clinical Neurophysiology*, vol. 106, no. 2, pp. 127–137, 1998.

[62] R. D. Pascual-Marqui, "Review of Methods for Solving the EEG Inverse Problem," *International Journal of Bioelectromagnetism*, vol. 5, no. 1, p. 25, 1999.

[63] P. C. Miranda, "Chapter 29 - Physics of effects of transcranial brain stimulation," in *Brain Stimulation* (A. M. Lozano and M. Hallett, eds.), vol. 116 of *Handbook of Clinical Neurology*, pp. 353–366, Elsevier, 2013.

[64] M. A. Jatoi and N. Kamel, "Brain source localization using reduced EEG sensors," *Signal, Image and Video Processing*, vol. 12, no. 8, pp. 1447–1454, 2018.

[65] V. Murzin, A. Fuchs, and J. Scott Kelso, "Detection of correlated sources in EEG using combination of beamforming and surface Laplacian methods," *Journal of Neuroscience Methods*, vol. 218, pp. 96–102, aug 2013.

Appendices

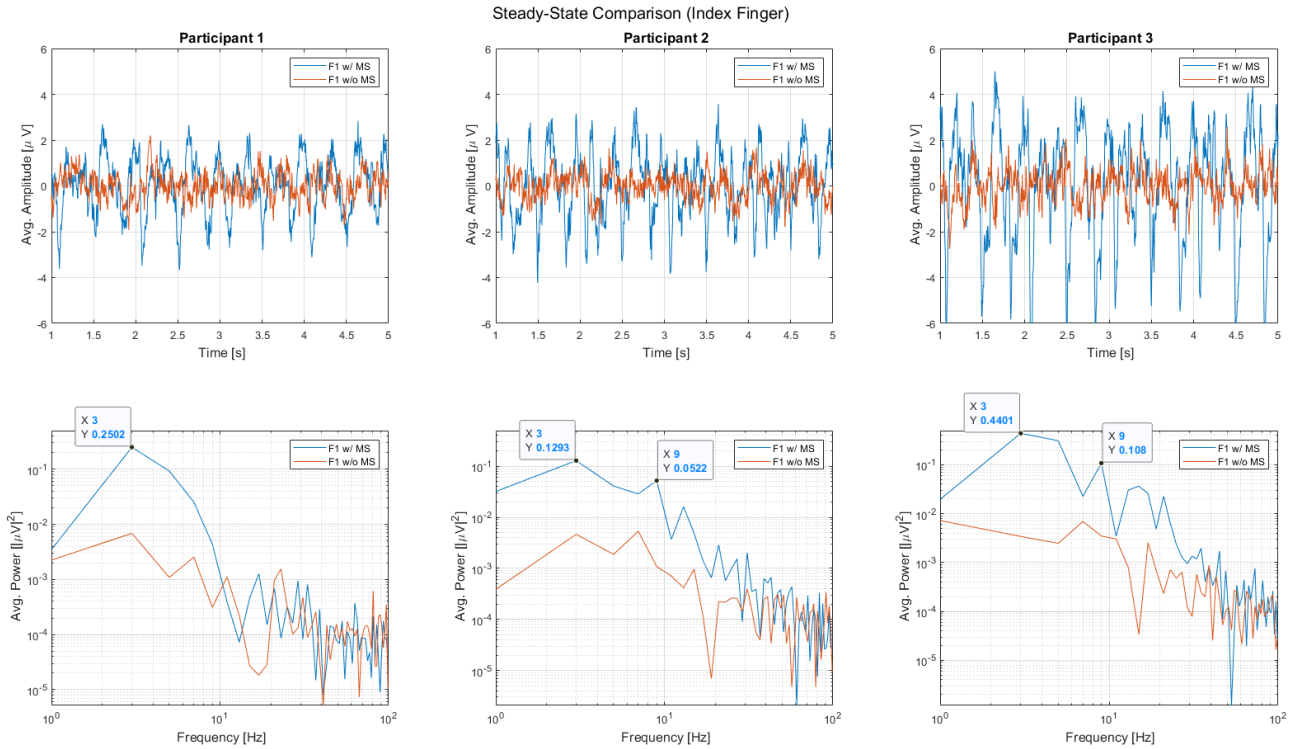

Figure 13: *The signal of the F1 EEG channel is averaged across trials and analyzed in time and frequency domains for all participants. A comparison is shown between the perturbed and the unperturbed conditions when participants used their index finger to control the lever. The oscillatory behavior of the blue signal is the response to the perturbation, as it is not present in the red signal. Two oscillatory peaks are pronounced at the* 3 *and* 9 *Hz frequencies.*

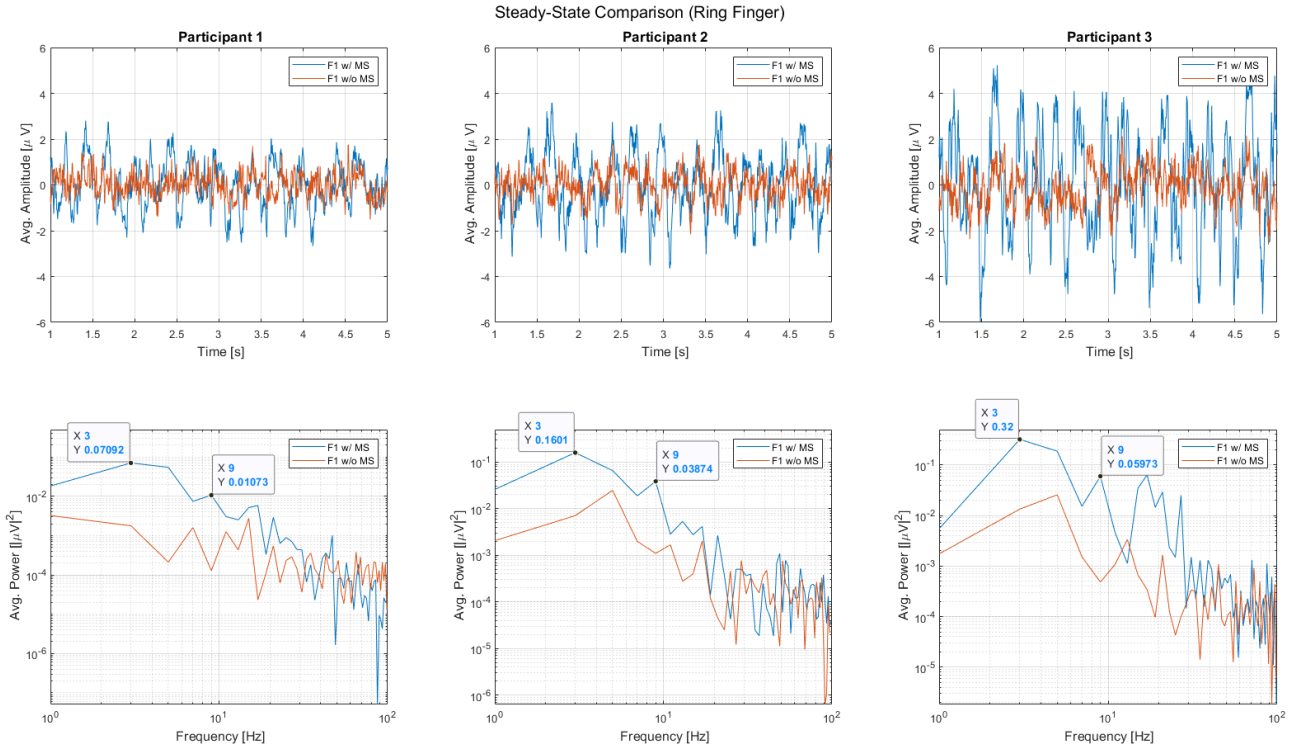

Figure 14: *The signal of the F1 EEG channel is presented as before. In this instance, the participants used their ring finger to control the lever. Similar results are reported.*

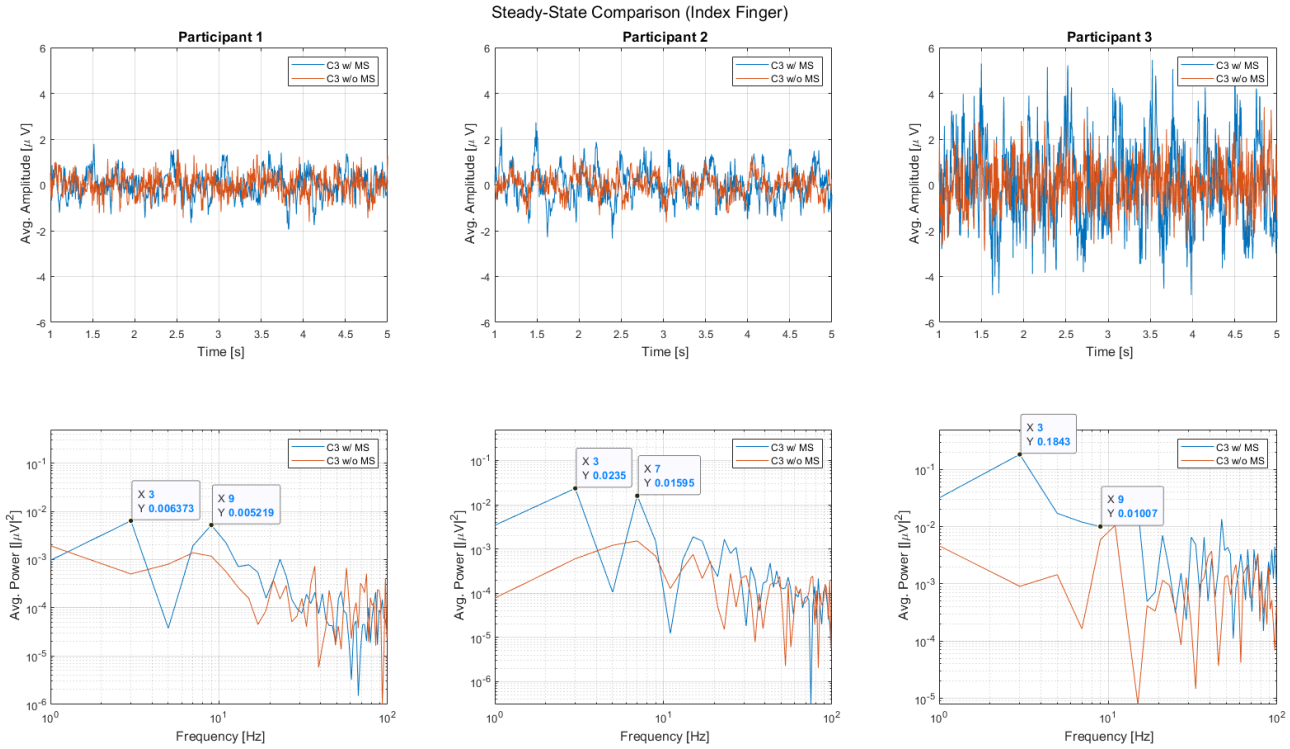

Figure 15: *The signal of the C3 EEG channel is averaged across trials and analyzed in time and frequency domains for all participants.*

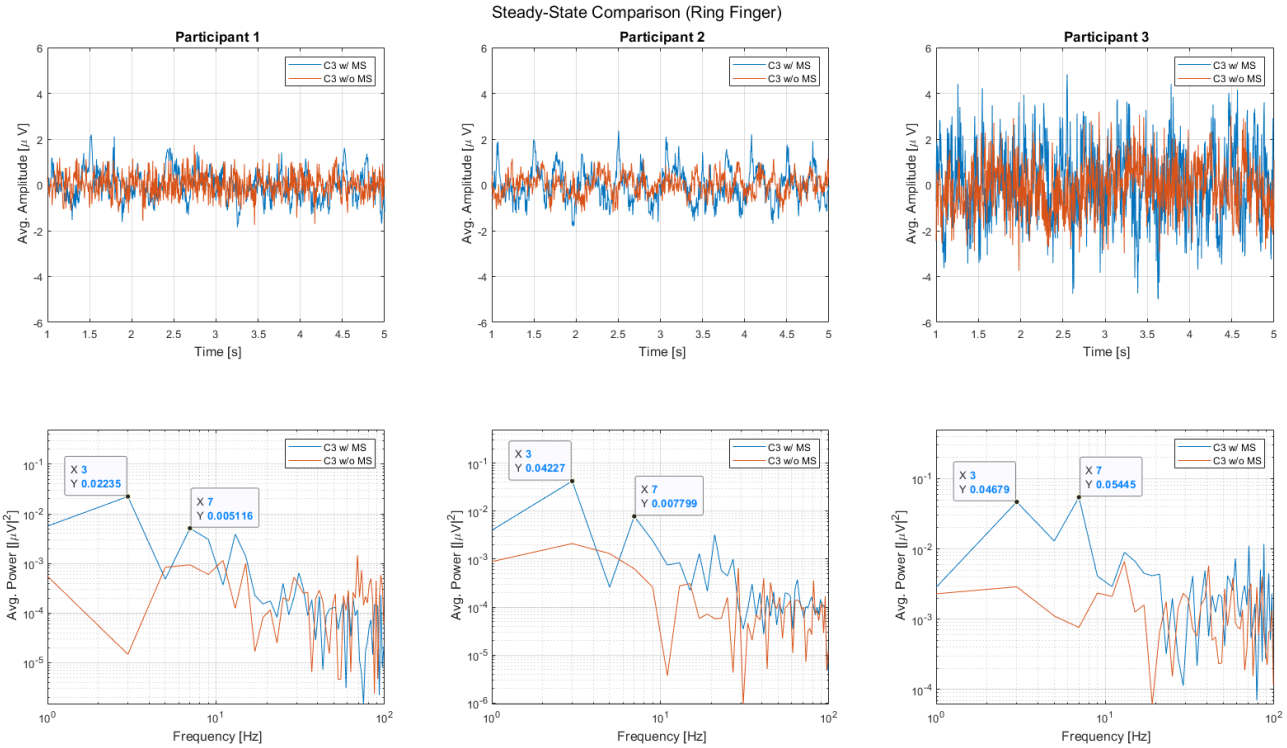

Figure 16: *The signal of the C3 EEG channel is presented as before. In this instance, the participants used their ring finger to control the lever. Similar results are reported.*

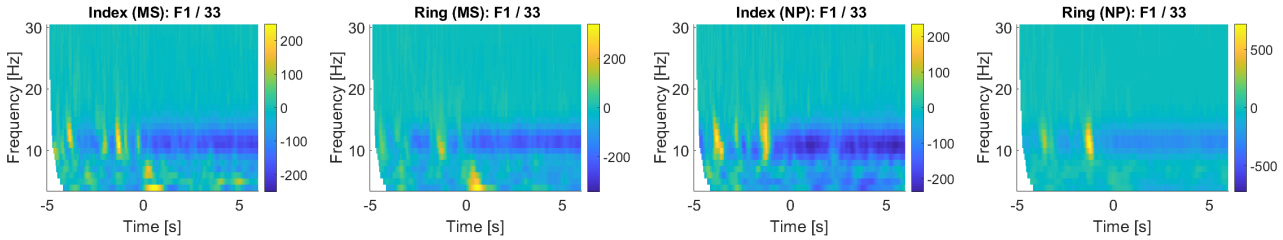

(a) *Participant #1*

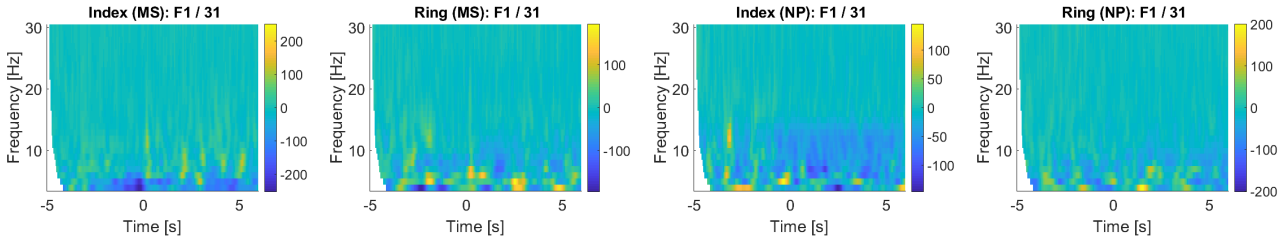

(b) *Participant #2*

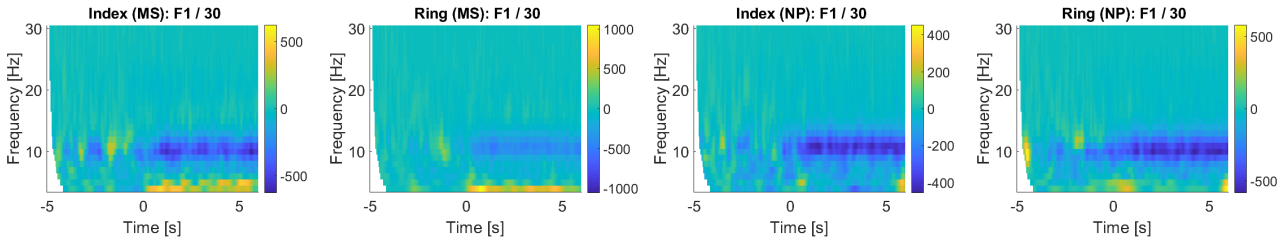

(c) *Participant #3*

Figure 17: *Time-frequency analyses of the data from the F1 channel for all conditions per participant. Each row shows the results of the analysis of the index and the ring fingers, starting with the two conditions with the perturbation and following with the results from the unperturbed conditions. Dark blue color indicates an absolute power drop relative to the chosen baseline time window of [-5 -3] seconds and a bright yellow indicates an absolute power increase relative to the same time window. The power values are expressed in $\mu W/Hz$. The maximum and minimum values are shown per condition in its respective color bar.*

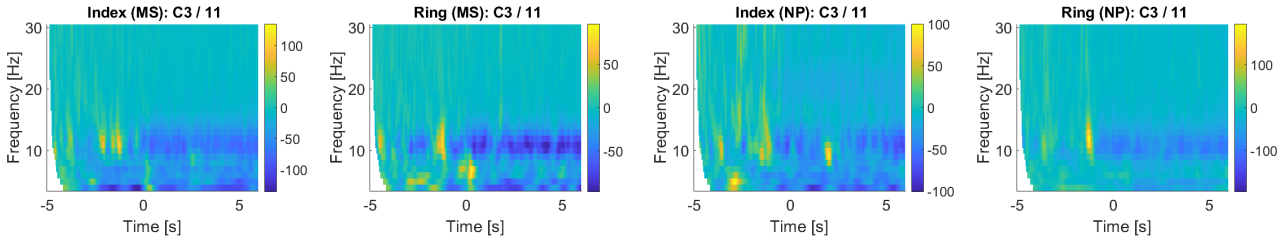

(a) *Participant #1*

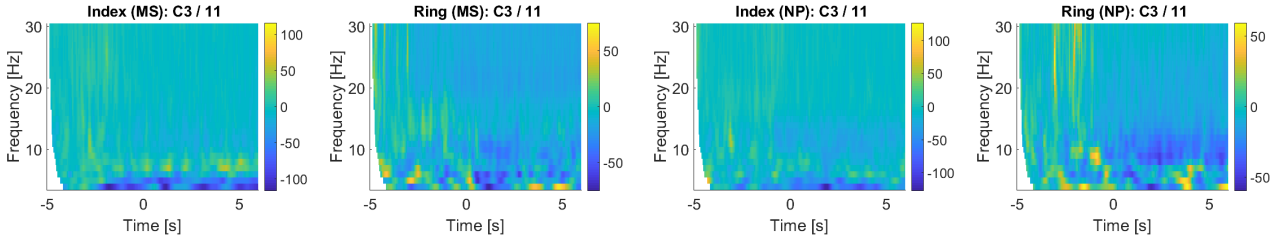

(b) *Participant #2*

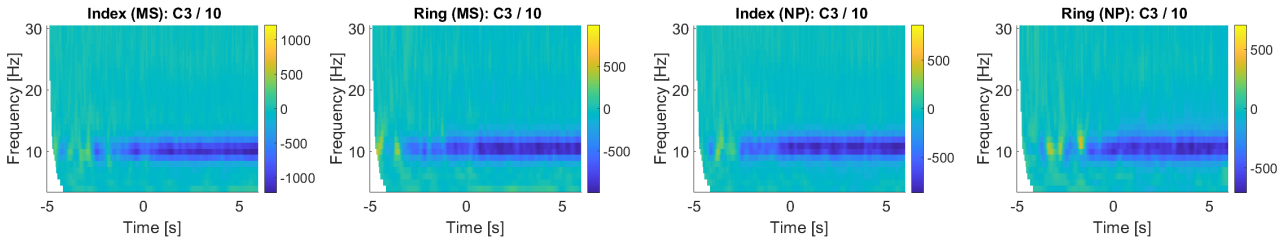

(c) *Participant #3*

Figure 18: *Time-frequency analyses of the data from the C3 channel for all conditions per participant. Each row shows the results of the analysis of the index and the ring fingers, starting with the two conditions with the perturbation and following with the results from the unperturbed conditions. Dark blue color indicates an absolute power drop relative to the chosen baseline time window of [-5 -3] seconds and a bright yellow indicates an absolute power increase relative to the same time window. The power values are expressed in $\mu W/Hz$. The maximum and minimum values are shown per condition in its respective color bar.*

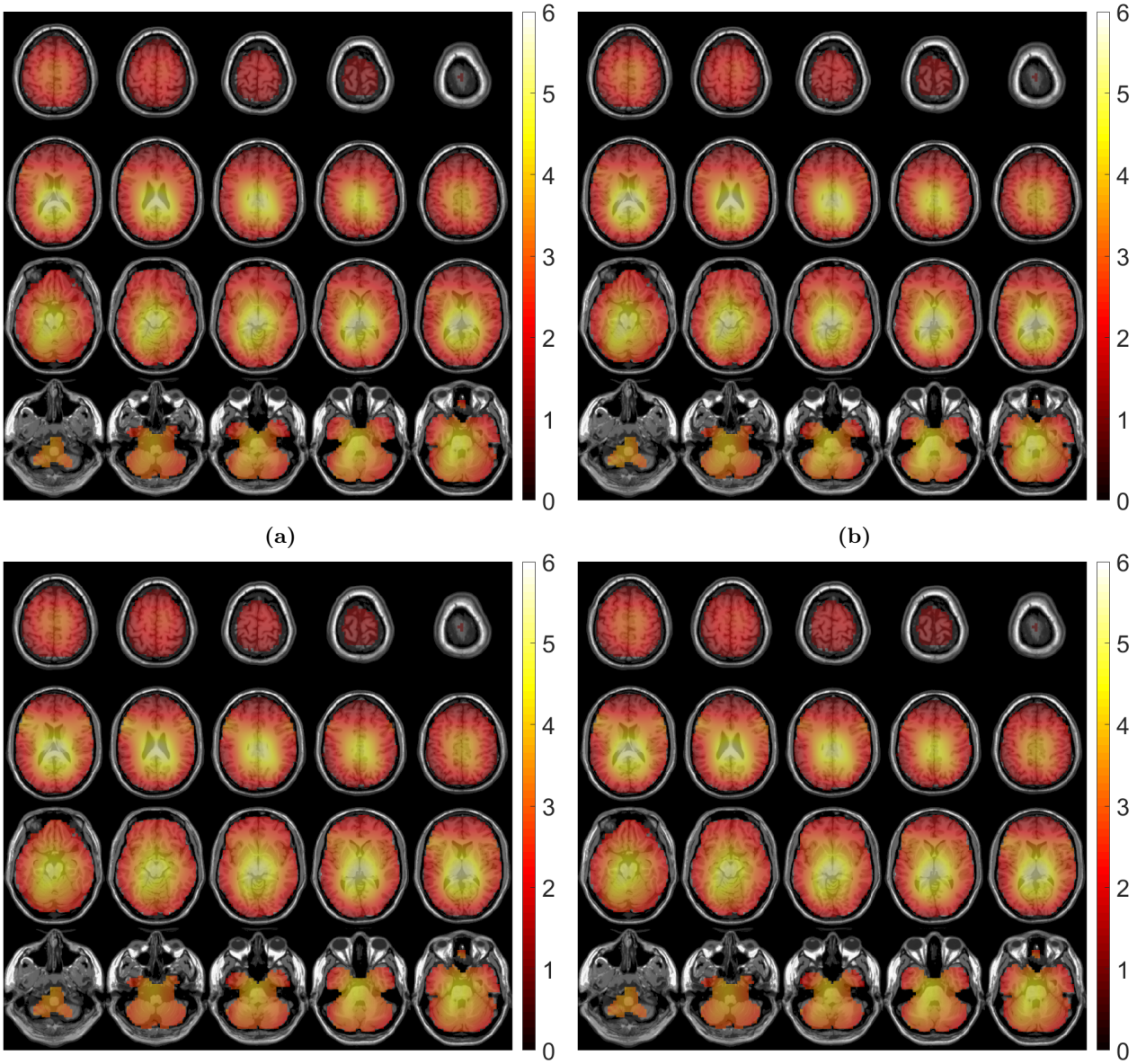

Figure 19: ***LCMV beamformer*** *source localization results. The results of the source localization are grand averaged over all participants per condition, without any applied masking. Figures (a) and (b) correspond to the perturbed conditions for the index and the ring fingers respectively. Figures (c) and (d) correspond to the unperturbed conditions, similarly arranged. Each figure is accompanied by a relevant color bar. Sources with higher power values are displayed with brighter colors; the power of the sources is given in a.u.*

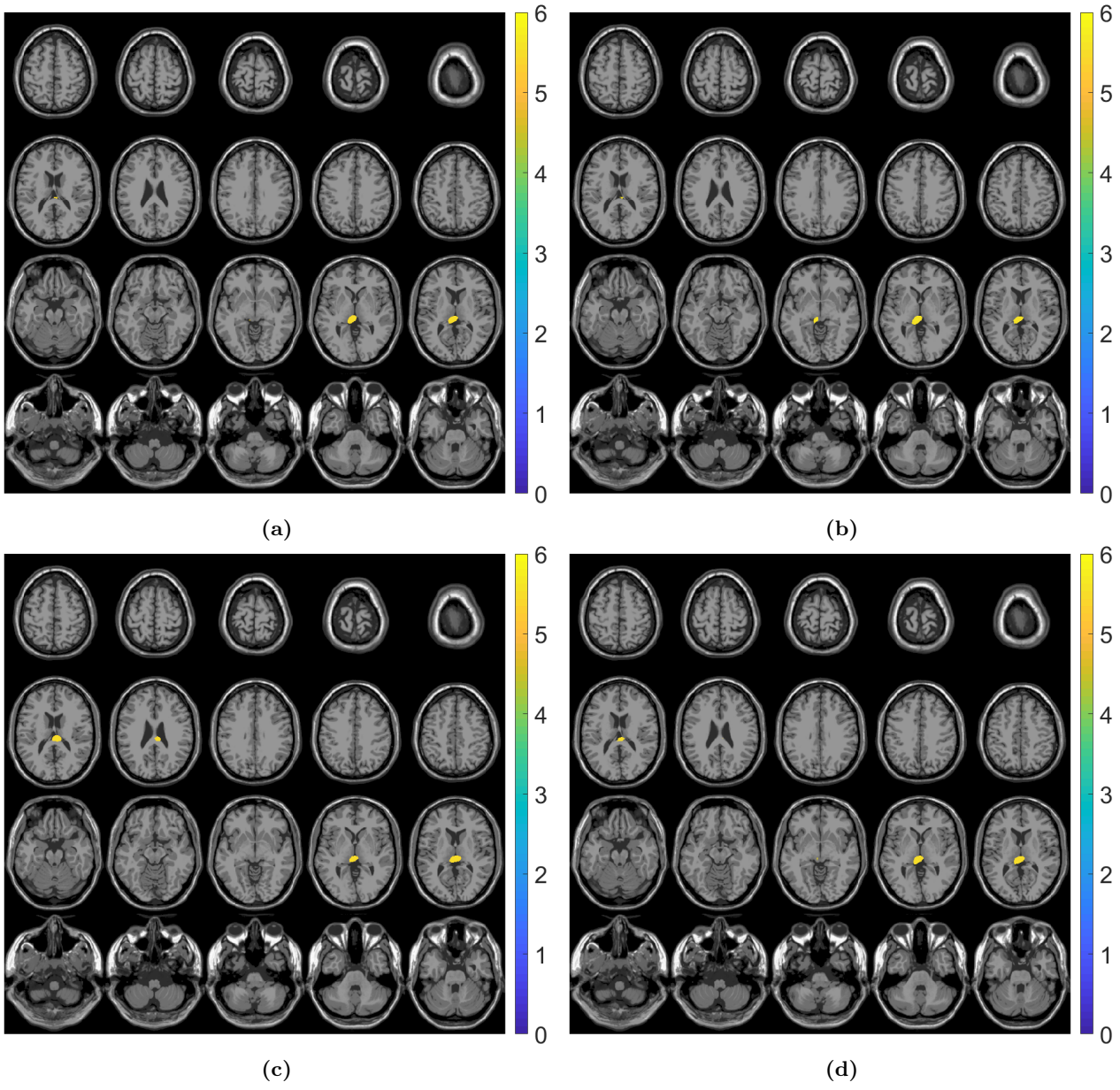

Figure 20: ***LCMV beamformer*** *results, after applying masking to isolate the sources that have power values in the top 2%. Just as before, the values of the sources are shown in a.u.*

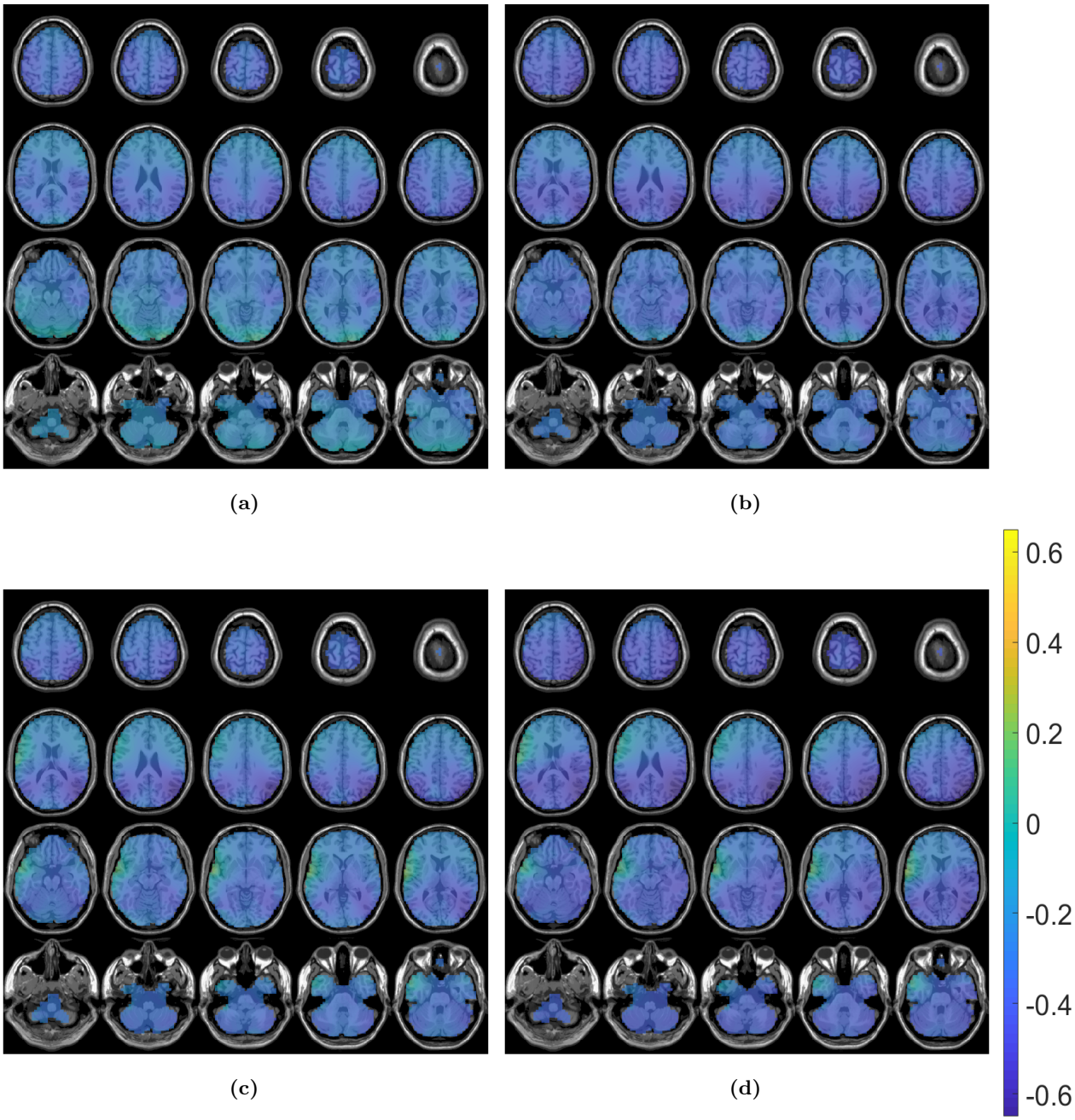

Figure 21: ***DICS beamformer*** *source localization results. The sources were localized based on the power in the alpha frequency band, centered around 10 Hz with a frequency smoothing of ±2 Hz. Power is normalized and contrasted between the steady-state time window* $t_{ss} = [1\ 5]$ *seconds and the pre-stimulus baseline* $t_{bsl} = [-5\ \ -1]$ *seconds where* $t_0 = 0$ *indicates the start of the trial. Positive values indicate a power increase during the steady-state in terms of the baseline; similarly, negative values indicate a power drop. The results were grand averaged over all participants per condition, without applying any masking. Each row corresponds to a different condition; the top row corresponds to the perturbed conditions and the bottom row corresponds to the unperturbed conditions. Figures (a) and (c) show the results when participants used their index finger. Figures (b) and (d) show the results when participants used their ring finger. The figures are all accompanied by a color bar indicating the color of the relative change between the baseline and the steady-state. Power values are shown in a.u.*

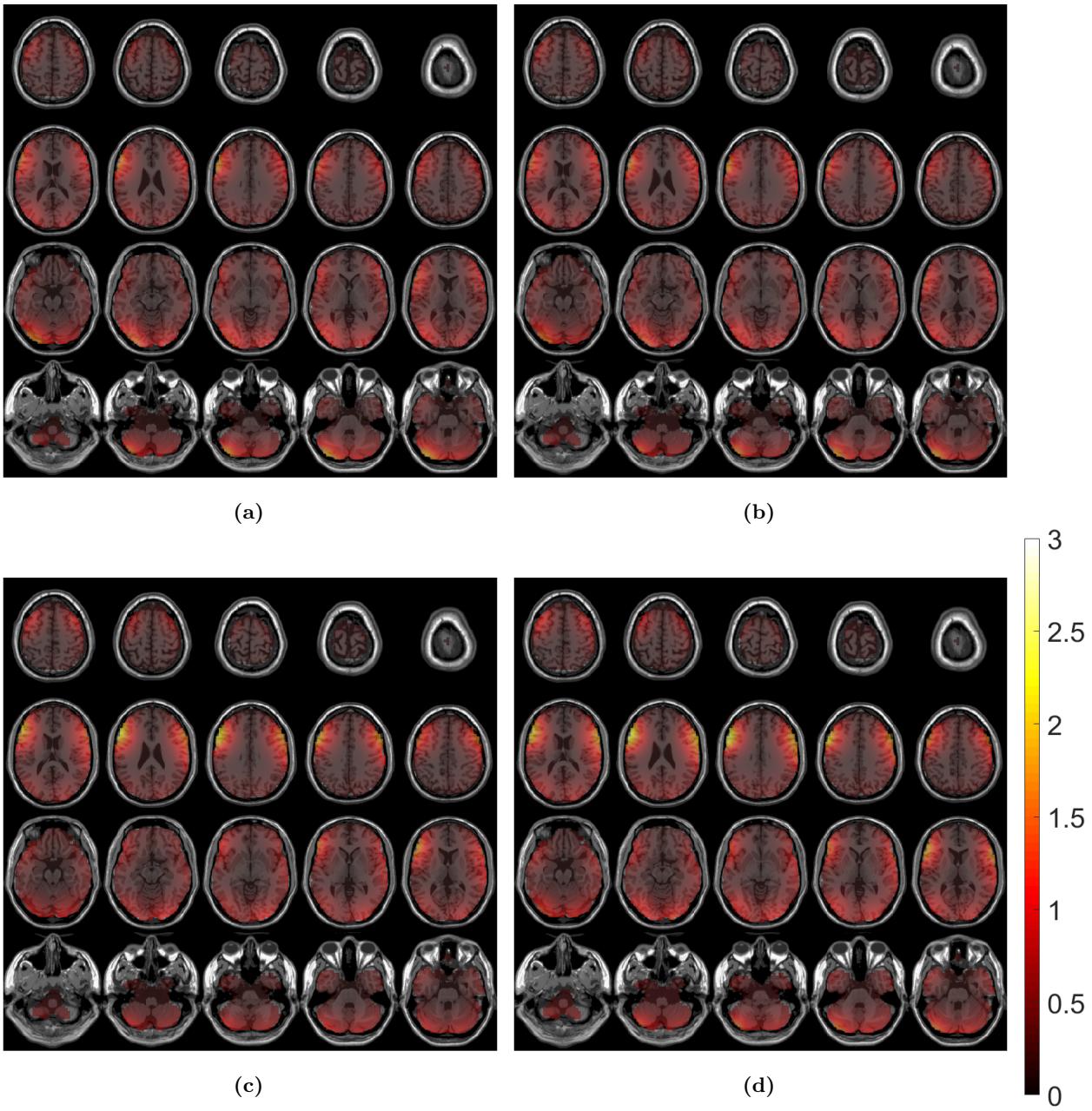

Figure 22: *Source localization results from the **sLORETA** method. The sources were localized based on the time-locked EEG signals during the steady-state time window $t_{ss} = [1\ 5]$. The instant $t = 0$ indicates the start of the trial. The results were grand averaged over all participants per condition, without any applied masking. Figures (a) and (c) show the results from using the index finger, with and without an applied perturbation respectively. Similarly, figures (b) and (d) show the results of using the ring finger. Figures are accompanied by a color bar indicating the strength of the localized sources. Highly-active sources are indicated with a brighter color. Source power values are shown in a.u.*

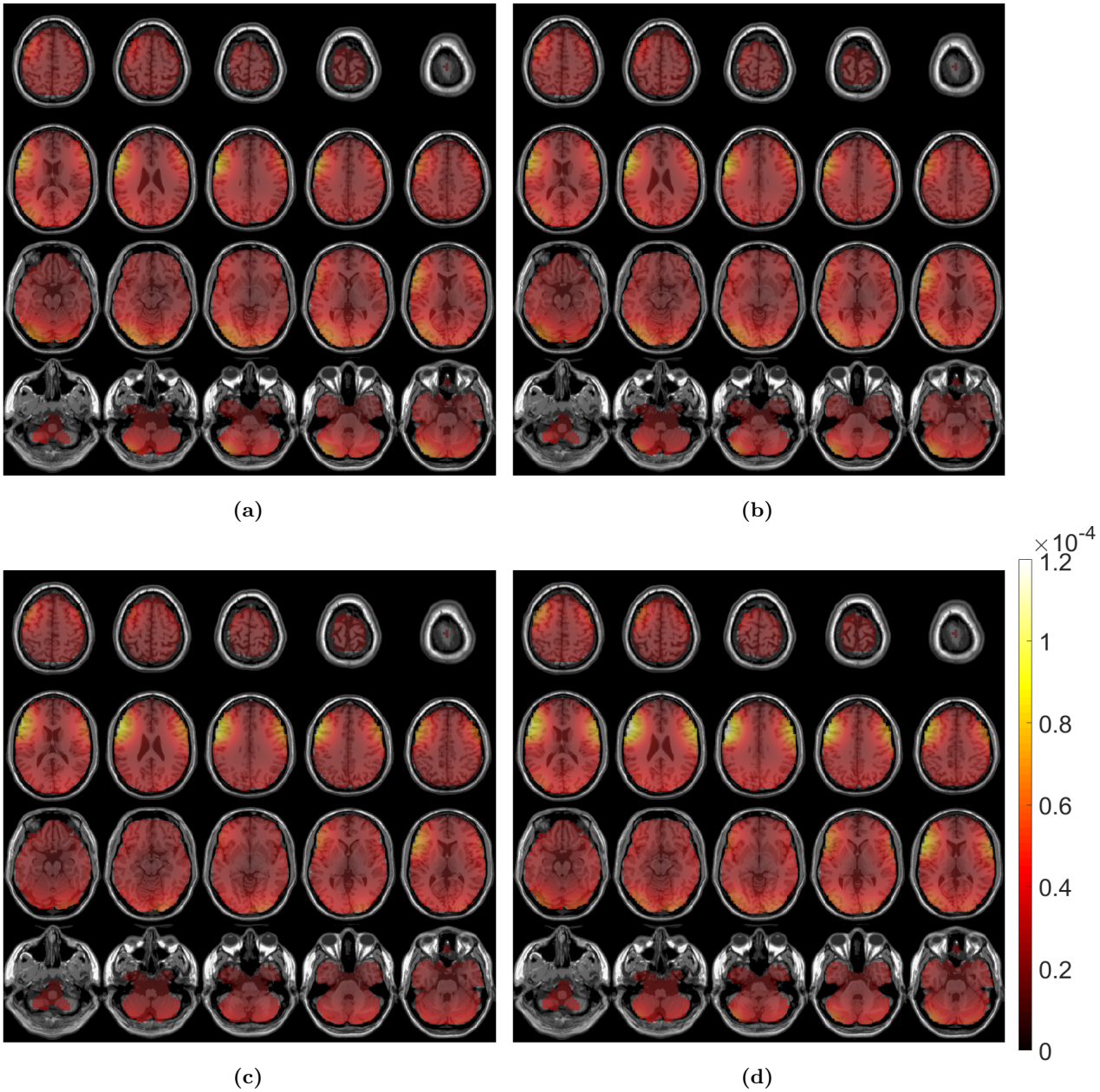

Figure 23: *Source localization results from the* ***eLORETA*** *method. The sources were localized based on the time-locked EEG signals during the steady-state time window* $t_{ss} = [1\ 5]$*. The instant* $t = 0$ *indicates the start of the trial. The results were grand averaged over all participants per condition, without any applied masking. Figures (a) and (c) show the results from using the index finger, with and without an applied perturbation respectively. Similarly, figures (b) and (d) show the results of using the ring finger. Figures are accompanied by a color bar indicating the strength of the localized sources. Highly-active sources are indicated with a brighter color. Source power values are shown in a.u.*